arXiv:2512.20506v1 [physics.app-ph] 23 Dec 2025

Ultrasonic metamaterial at MHz frequencies using microstructured glass

Oscar Demeulenaere[1,2*], Nikita Ustimenko[3], Athanasios G. Athanassiadis[1,2], Lovish Gulati[1,2], Carsten Rockstuhl[3,4], Peer Fischer[1,2,5,6],

[1] Max Planck Institute for Medical Research, Jahnstr. 29, 69120 Heidelberg, Germany

[2]Institute for Molecular Systems Engineering and Advanced Materials, Heidelberg University, Im Neuenheimer Feld 225, 69120 Heidelberg, Germany

[3]Institute of Theoretical Solid State Physics, Karlsruhe Institute of Technology, Kaiserstr. 12, 76131 Karlsruhe, Germany.

[4]Institute of Nanotechnology, Karlsruhe Institute of Technology, Kaiserstr. 12, 76131 Karlsruhe, Germany.

[5]Center for Nanomedicine, Institute for Basic Science (IBS), Seoul 03722, Republic of Korea.

[6]Department of Nano Biomedical Engineering (NanoBME), Advanced Science Institute, Yonsei University, Seoul 03722, Republic of Korea.

[*]Corresponding author. Email: oscar.demeulenaere@mr.mpg.de

Acoustic metamaterials enhance traditional material properties through microstructure engineering, providing new opportunities to shape sound fields in applications ranging from biomedical imaging, clinical therapy to non-destructive testing. However, at the MHz frequency ranges, only a few metamaterial architectures exist. They are often highly attenuating or difficult to manufacture, and generally provide limited 3D control over sound propagation. Here, we intro-

duce a MHz-frequency ultrasonic metamaterial based on laser-engraved glass. By structuring meta-voxels with different engraving patterns, we define a fully-3D, anisotropic metamaterial exhibiting local variations in the sound speed of up to 20% compared to unstructured glass, and losses 100× lower than in comparable 3D printed metamaterials. We use this metamaterial to define a library of standard elements that can be modularly combined to create and shape complex-patterned ultrasonic fields. Our experiments are supported by a theoretical model, which provides additional insights into the microstructural origin of the metamaterial behavior and opens the door to designing tailored ultrasound fields and responses.

Introduction

The ability to precisely shape ultrasonic wavefronts is critical for diverse biomedical and engineering applications. In medicine, MHz-frequency ultrasound offers deep tissue penetration with millimeter-scale focusing, making it indispensable for noninvasive imaging and therapeutic interventions. Wavefront shaping in these contexts enables the correction of aberrations introduced by heterogeneous media and precisely localizes ultrasonic energy for imaging or therapeutic techniques such as transcranial neuromodulation (*1*) and thermal ablation (*2*). Emerging applications in acoustofluidics leverage patterned ultrasound fields for particle sorting and microassembly (*3*), tissue engineering (*4*), and even 3D printing (*5*). Industrial testing similarly benefits from the high precision and long propagation distances of MHz-frequency ultrasound (*6*). In such applications, deliberate scattering masks and dispersion engineering can provide additional information about complex structures being imaged (*7, 8*). Finally, approaches to physical computation can benefit from new techniques to fabricate intricate 3D structures for acoustic wavefront control (*9*).

Typically, ultrasonic wavefronts are either actively shaped using phased arrays or passively shaped using phase-modulating elements such as lenses or holograms (*7*). Ultrasonic phased arrays are the gold standard for imaging applications, but do not scale well to the large element counts needed to project complex fields, due to the increasing hardware complexity and cost of the required driving electronics. In many cases, it is more effective to control ultrasonic wavefronts using passive phase-modulating elements paired with single-element transducers. A common technique relies on

phase plates fabricated from polymers whose sound speed differs from that in the surrounding (typically water-like) medium. By appropriately designing the phase plate thickness, a phase shift can be introduced to the impinging wavefront, giving rise to a complex pressure field pattern in the desired focal region (*10*). However, polymeric phase elements typically exhibit high absorptive losses that introduce limitations for use with high-power sources (*11*) or for use in complex field shaping using 3D volumetric holograms (*12*).

An alternative approach for wavefront engineering that offers even more degrees of freedom is to use acoustic metamaterials. Metamaterials are microstructured materials comprised of subwavelength unit cells, whose collective influence on an incident wave gives rise to diverse properties, including many that cannot be realized in traditional homogeneous materials. In addition to providing tunable sound speeds, metamaterials allow wave propagation to be designed in more complex ways, including anisotropic (*e.g.*, birefringent), dispersive (frequency-dependent), and topologically-guided behaviors (*13*). Despite such promise, however, the availability of metamaterial architectures that function at MHz frequencies is limited by challenges in fabrication and scaling. Conventional acoustic metamaterial architectures, such as elastomer composites (*14, 15*), labyrinthine structures, micro-pillars, or Helmholtz resonators (*16*), form a powerful toolbox for engineering low-frequency devices, but have not been effectively scaled for use at MHz frequencies. Experimental realizations in the MHz regime include silicone-based gradient-index metasurfaces (*17*) for broadband focusing and beam steering, and lithographically-manufactured planarized micropillar arrays that precisely modulate the phase shift across a thin structure for acoustic holography (*18*).

However, such current approaches face several limitations. While microfabrication techniques are suitable for small devices, producing accurate structures to modulate large-area sources (*e.g.*, > 5 cm), such as those relevant in many higher-power applications, remains limited by manufacturing costs and alignment errors. Another limitation arises when the material in use exhibits high acoustic losses at MHz frequencies. 3D-printed photopolymers such as VeroClear (Stratasys Inc) that are typically used for 3D printed phase plates, have an attenuation of 370 dB $\mathrm{MHz}^{-1}\,\mathrm{m}^{-1}$ at 2 MHz (*19*), which is orders of magnitude higher than that of other typical ultrasonic propagation materials (Table 1). Other metamaterials based on silicone similarly exhibit high attenuation at MHz frequencies (*20*). Beyond just limiting power delivery to the target, high attenuation introduces

heating that can lead to detrimental effects in high-power applications, such as changes in sound speed and geometric warping, which are known to reduce the performance of phase plates (*21*).

To overcome such limitations, we introduce here a new low-loss and scalable metamaterial architecture based on microstructured glass capable of shaping ultrasound wavefronts at MHz frequencies. By using glass as the underlying substrate, our metamaterial architecture benefits from the extremely low ultrasonic losses (*22*), high structural stability, and high thermal stability of glass. BK7 glass is micromachined using subsurface laser engraving, a 3D laser processing technique that creates individual, 100-µm scale microcracks at precisely defined locations within the glass. Such an approach was previously explored to manufacture artificial flaws for calibration of non-destructive testing probes and was shown to exhibit scattering and shear-wave birefringence (*23*) in the MHz frequency range. Here, we substantially build on these early results to pattern arbitrarily shaped metamaterial regions within large (cm-scale) glass volumes to manipulate ultrasonic waves in 3D.

We characterize the effective properties of a laser-engraved voxel consisting of thousands of microcracks that are much smaller than the wavelength. We measured the effective speed of sound and density of one voxel using a refracto-vibrometry technique. Notably, we observed that the effective sound speed is strongly anisotropic, which we relate to the microcrack geometry. The response is also highly frequency-dependent, pointing to resonant interactions within the metamaterial. We introduce and experimentally validate a numerical transition-matrix (T-matrix) model (*24–26*) describing the metamaterial, which allows the scattering properties of an arbitrary pattern of microcracks to be accurately predicted based on the scattering characteristics of a single microcrack. This T-matrix approach also confirms the metamaterial nature of this engraved material.

Building on the characterization of the metamaterial unit cells, we designed distinct elements to control the ultrasonic wavefront inside the glass: a lens, a grating, a waveguide, and several holograms, all of which exhibit very low attenuation in the MHz frequency range. Finally, we highlight the modularity of this platform by combining individual metamaterial components to create more complex acoustic wavefront shaping systems, reminiscent of complex optical assemblies based on fundamental elements.

Results

Micro-engraved glass constitutes a tunable MHz-frequency metamaterial

To create our metamaterials, 3D patterns of microcracks were machined on the inside of 5 cm glass cubes using commercially available subsurface laser engraving services (M+B Lasertechnik GmbH). Through this process, a 532 nm pulsed laser is focused precisely to user-selected positions inside the glass via computer-controlled adjustable lenses, inducing localized thermal stresses that produce micro-fractures without damaging the bulk medium (Fig. 1). For our most commonly used machining parameters, the microfractures have typical diameters of 39 ± 4 μm perpendicular to the machining laser axis (x- and y-axes) and lengths of 211 ± 21 μm along the laser axis (z-axis). An example of the complex patterns possible with this technique is shown in Fig. 1A.

By patterning the cracks, a tunable phase shift could be introduced to an incident compressional wave in the glass, due to a change in the effective sound speed of the micropatterned region. The unmodified glass blocks have a density of $\rho_0 = 2525 \pm 8$ kg m^{-3} and a longitudinal speed of sound of $v_0 = 5816 \pm 4$ m s^{-1} (see Materials and Methods). Values were in good agreement with the literature for BK7 glass, which is a typical glass material used in subsurface laser engraving (*22*). These baseline acoustic properties were then compared with the effective sound speed and density of rectangular meta-voxels within an otherwise homogeneous glass block. Meta-voxels consisted of $45 \times 45 \times 115$ microcracks arranged in a 3D rectangular grid spanning $4 \times 4 \times 31$ mm^3.

To measure the effective medium properties, pulsed compressional waves with a center frequency of $f_0 = 2.25$ MHz were incident on the sample, and the wave propagation within the glass block was observed using refracto-vibrometry (Fig. 2A). By combining the known length of the metavoxel and the measured transit time of the pulse through the metavoxel, we were able to measure the effective compressional wave speed of the metavoxel. Then, using the effective sound speed along with the reflected wave amplitude from the metavoxel, we could measure its effective density. These measurements were repeated for incident waves along all three principal axes of the metavoxel (x, y, and z), where the long axis of the voxel was always parallel to the vibrometry axis (see Materials and Methods).

These measurements revealed that the patterned microcracks reduce the effective sound speed in the glass by up to 20% and increase the effective density by up to 20% (Table 2). This effect,

however, is anisotropic, only appearing along the x-axis.

While a difference in effective medium properties in the z-direction is expected because of the extended crack length along the laser propagation direction, the difference between the x- and y-direction is surprising because of the rotational symmetry of the laser beam. To understand the origin of this birefringent behavior, we studied the microcrack geometry using a light microscopy. We observed that microcracks do not have the same geometry along the x- and y-axis (Fig. S1), with more irregular shapes appearing along the y-axis. This asymmetry is nonetheless uniform from crack-to-crack and sample-to-sample, suggesting a reproducible instability in the laser-matter interactions at the focus as the origin.

Using the crack geometry as a fundamental scatterer, we built a numerical model to explore the metamaterial behavior more generally using a linear transition-matrix (T-matrix) approach. In short, the scattering behavior of a single microcrack was described analytically in the frequency domain, assuming a subwavelength ellipsoidal scatterer with anisotropic material parameters located in the unbounded, homogeneous medium, which is the bulk glass medium (see Materials and Methods). In this regard, the acoustic response of the microcrack is completely determined by its T-matrix, allowing us to predict wave propagation behavior through arbitrary arrangements of cracks, accounting for multiple scattering and mutual crack-crack interactions.

The scattered field predicted by this method for a 3D grid of microcracks shows excellent agreement with the refracto-vibrometry data (Fig. 2D). As these 2D vibrometry measurements are projections of the 3D acoustic field inside the glass, we applied a quasi-averaging procedure to the numerical results to simulate the expected measurement data. Along with the pressure field pattern, the effective speed of sound and density from the simulation results exhibit excellent quantitative agreement with the experimental results (Fig. S2). The T-matrix simulation is also able to predict the effective sound speed as a function of crack spacing (Fig. S3). Moreover, the T-matrix predictions accurately capture the anisotropic properties of the metavoxels with high accuracy using only a monopole-dipole approximation, revealing that the metamaterial behavior arises primarily from the strongly anisotropic dipole response of a standalone microcrack.

The combined experimental and numerical results on the metavoxel sound speed demonstrate the metamaterial nature of the microstructured glass: the strong scattering behavior of individual, deeply-subwavelength microcracks gives rise to an emergent effective medium at wavelength-

scales and above. As is commonly observed in metamaterials, we observe that the effective medium properties in the microstructured glass metavoxels are highly frequency-dependent. A difference between the longitudinal speed of sound inside the bulk and the effective medium is only seen in a frequency window close to 2.25 MHz. At 0.5 and 5 MHz, no difference was observed between the two media (Fig. S4).

Finally, we measured the attenuation of compressional waves in a metavoxel and found that the attenuation coefficient of the microstructured glass metamaterial is exceptionally low. Whereas the bulk glass exhibits an attenuation of $\alpha = 3.3 \pm 0.4$ dB m^{-1} MHz^{-1}, in good agreement with previous reports (*22*), we find the microstructured glass to exhibit isotropic attenuation only 10% higher than the bulk glass (Fig. S5). For comparison, polymers and other materials commonly used for ultrasonic wavefront shaping exhibit attenuation coefficients 100× higher in the MHz frequency range (Table 1).

Microstructured glass metamaterial can be patterned for modular, arbitrary wavefront shaping

Because of its ease of manufacturing, control over sound speed, and low losses, we use our metamaterial to create a library of wavefront-shaping elements made of glass. All elements were laser engraved into $5 \times 5 \times 5$ cm^3 glass blocks (Fig. 3). To illustrate the variety of elements that can be achieved, we manufactured a focusing lens, a grating, a waveguide, and multi-focus holograms. Using both refracto-vibrometry through the glass and surface vibrometry at the face opposite the transducer, we observe excellent control over the 2.25 MHz acoustic wave propagating inside the glass.

Among the benefits of using glass for wavefront shaping are its high structural and thermal robustness (Table S1) and its corresponding ability to withstand high acoustic powers. Tests of our elements in acoustic fields of increasing power revealed no structural damage or wavefront aberration with increasing power, up to a maximum intensity of 20 $W\,cm^{-2}$ that our transducer could transmit.

Another major benefit of glass block meta-elements is their ability to couple sound effectively through their flat faces. Beyond general coupling, this opens the door to modularity by stacking and rearranging elements face-to-face. (Fig. 4). To demonstrate these strengths, we composed

different wavefront manipulations sequentially to demonstrate more complex acoustic wavefront manipulations. For instance, by coupling a Fresnel lens block to a grating block using water-based coupling gel and slight compressional pressure between the blocks, a dual focus element could be realized with minimal energy loss at the block interface (Figs. 4 and S6). Moreover, these phase-transforming elements can be rearranged and replaced flexibly, in a manner that is common in optical assemblies but has not previously been demonstrated for MHz-frequency ultrasound.

Discussion

Here, we have introduced a metamaterial architecture for MHz-frequency ultrasound based on microstructured glass. By patterning sub-wavelength laser-induced microcracks in regular grids, it is possible to simultaneously lower the effective sound speed and raise the effective density of the glass by up to 20%. This allows for manipulations of incident ultrasonic wavefronts with minimal reflections at the metamaterial interface. The metamaterial's effective properties arise from multiple-scattering interactions between the cracks, which we capture theoretically using a T-matrix formalism. Numerical predictions using our T-matrix framework demonstrate excellent agreement with experimental results, and it captures the anisotropic behavior of the metamaterial arising from the micro-crack response. The numerical formalism provides a method for further exploring the design space of these metamaterials, including how microstructure patterns can be designed to achieve specific effective properties.

At MHz frequencies, few metamaterial architectures have been developed, and many traditional architectures that work well at lower frequencies do not scale well because of losses and manufacturing limitations. The approach presented here overcomes these issues by leveraging a natively 3D microfabrication tool to directly modify a low-loss substrate (glass). In comparison with other common MHz-frequency metamaterials, such as elastomer composites or steel-rod phononic crystals (*27*), this approach offers numerous advantages. Microstructured glass can be used to create truly 3D metamaterials from a mechanically- and thermally-stable material. By embedding the metamaterial in glass blocks with flat faces, metamaterial devices can easily be index-matched to ambient conditions using standard index-matching layers. Moreover, it is possible, using laser refracto-vibrometry, to directly interrogate the ultrasonic fields inside the material to help drive

the development and optimization of metamaterial devices. In contrast with other microstructured metamaterials based on 3D printed polymers (*28*), the metamaterial we introduce exhibits extremely low losses at MHz frequency, and is stable up to high intensities of 20 W/cm^2. These advantages provide new opportunities to develop metamaterial-based ultrasonic devices at MHz frequencies.

One of the promising directions in which the metamaterial can provide new capabilities is for complex 3D wavefront shaping. Because of the manufacturing method and the deep-subwavelength size of the fundamental scatterers, the metamaterial can easily be spatially patterned in 3D for complex wavefront engineering. We demonstrate this by creating a library of patterned metamaterial blocks that perform diverse wavefront shaping functions, including focusing, diverting energy into grating lobes, and patterning sound using a hologram. We are not aware of any metamaterial system to date that has been used for such general wavefront manipulations at MHz frequencies. Moreover, the metamaterial architecture is highly modular, and the fundamental blocks can be combined in different ways to produce wavefront-shaping assemblies. Such assemblies are commonplace in optics, and they have provided the flexibility to define intricate and diverse optical experiments, yet such acoustic elements have not been previously developed for ultrasound. Microstructured glass can therefore provide significant opportunities to develop customized wavefront shaping systems, particularly for high-power applications, including contactless ultrasonic power transfer (*29*), therapeutic focused ultrasound for ablation and hyperthermia (*2*), and manufacturing (*5*).

Beyond conventional applications of wavefront shaping, microstructured glass offers unique benefits that could facilitate easier and more widespread realization of new MHz-frequency ultrasonic devices. In particular, the 3D patternability, high sound speed, and low losses together make the metamaterial particularly appealing for potential applications in ultrasonic signal processing and computing (*9*), especially in opening the door to volumetric ultrasonic neural processing.

Materials and Methods

Characterization of the bulk glass material

Glass samples were ordered from the company *M+B Lasertechnik GmbH*. Most ordered glass blocks were cubes with an edge length of 50 mm. Three control cubes, *i.e.*, without any engraving, were studied first. Their density was measured by weighing them and measuring their volume. The

longitudinal speed of sound was measured with an Olympus transducer with a diameter of 1.5 inches (38.1 mm) and with a center frequency of 2.25 MHz. A refracto-vibrometry technique was used to measure the time-of-flight. A schematic (Fig. S7A) and a picture (Fig. S8A) of the setup are depicted. For more details on the refracto-vibrometry measurement, see (*30*). From a 5-cycle burst at 2.25 MHz, time-of-flights t_1 and t_2 were measured at one position but for several time subsets corresponding to different reflections of the burst from the bottom face of the cube (Figs. S7B and C). The longitudinal speed of sound was calculated as

$$v_0 = \frac{2L}{t_2 - t_1} \,. \tag{1}$$

Multiple points along the propagation direction were measured using the same protocol to obtain independent data points and assess the variability of the speed of sound measurements. Refracto-vibrometry provides a 2D projection of the 3D acoustic field, and therefore does not directly capture the full spatial pressure distribution. We used a standard pulse-echo measurement to validate the robustness of the refracto-vibrometry approach for speed of sound measurement. The same transducer was connected to a pulser-receiver along with an oscilloscope (Fig. S7D). By measuring the time-of-flights t_1 and t_2 of two consecutive amplitude peaks of the obtained time signal, *i.e.*, two consecutive reflections, we calculated the speed of sound using Eq. (1). Several consecutive peaks were used to obtain independent data points. The speed of sound measurement gave a 0.1 % difference (relative ratio) with the measurement from the refracto-vibrometry.

Finally, we measured the attenuation of this glass material at several MHz frequencies. For this, we used a bigger block of size $70 \times 70 \times 250$ mm to increase the propagated distance between consecutive reflections. We used the same pulse-echo setup (Fig. S5A) with transducers whose center frequencies are 2.25, 5, and 10 MHz. The detected absolute maximum amplitude for each reflection was plotted over propagation distance, knowing the speed of sound (Fig. S5B). The slope of a linear fit at each frequency provided the attenuation. Another linear fit was used to derive the attenuation per MHz.

Characterization of engraved glass area as an anisotropic effective medium

Once the bulk glass material had been characterized, we investigated the properties of the engraved area. For that, we considered a sample with one engraved metavoxel of size $4 \times 4 \times 31$ mm consisting

of a regular 3D lattice of microcracks (Fig. 2A) and compared it to a control block. The metavoxel was elongated along one direction because the refracto-vibrometry measurement is a 2D projection of a 3D field. The metavoxel had to be long enough along the optical path length of the vibrometer's laser to give a meaningful measurement. A 3D-printed base allowed for the placement of both glass cubes at the same position (Fig. S8A). Using refracto-vibrometry, we measured the time-of-flight between two scanning points for both blocks. Considering the engraved area as an effective medium, we calculated the effective speed of sound and density for each propagation direction from the time-of-flight data (Figs. 2C and S9). For more details on the calculation of the effective speed of sound and density, see (*30*). Finally, we measured the attenuation inside the engraved area. Three large cylinders were engraved along the x, y, and z axes in different glass cubes. We used the same approach as mentioned above to measure the attenuation for each of them at 2.25 MHz.

T-matrix simulation

To calculate the scattered pressure field of microcrack patterns and also evaluate their effective parameters, we used a T-matrix-based approach that has been implemented in an openly available Python package *acoustotreams*, v.0.2.5. This full-wave simulation approach considers the microcracks as anisotropic ellipsoids in the quasistatic approximation and computes their linear acoustic response by expanding incident and scattered pressure fields in scalar multipole waves, including only the monopole and the dipole. The T-matrix, which can analytically account for mutual interactions among multiple microcracks, directly maps the incident coefficients to the scattered ones, enabling efficient and accurate predictions for multiple patterned microcracks (Fig. 2D). For more details on the T-matrix approach, see (*30*).

Design and measurement of a few metamaterials

Once we had characterized experimentally and theoretically an engraved voxel as an anisotropic effective medium, we designed several elements to shape the ultrasound wavefront inside the glass block. We designed standard elements such as a biconvex converging lens, a 3D cylinder acting as a waveguide, and a 1D grating (Fig. 3B-D). For every engraved 3D shape, a 3D point cloud was generated to fill in the shape with points with a spacing of $[90, 90, 270]$ μm. The list of coordinates x, y, and z of these millions of points was then sent as a text file to the company for engraving. A

pulse laser of wavelength 532 nm was then directed along the z direction for every point to generate a microcrack. For more details on the laser engraving step, see (*30*). To measure the field, we used the same refracto-vibrometry technique again. It is then possible to plot the 2D time field from the signal measured by the vibrometer. We also computed the Fast Fourier Transform (FFT) of the measured signal with a time window covering the propagation of the burst in the field of view. The amplitude of the FFT output was plotted to describe the field.

Design and measurement of holograms

Phase plates were designed and engraved inside the glass (Fig. 3). They were located 4 mm away from the face in contact with the transducer and with a similar diameter. One hologram was designed to output two foci at different depths along the propagation axis simultaneously (Fig. 3E). The same refracto-vibrometry technique was used to measure the field. A longer ultrasound burst of 10 cycles was transmitted instead of 5 cycles. Several phase plates were designed so that the image plane was located at the cube face opposite the transducer (Fig. 3G-I). This time, a conventional surface vibrometry technique was performed. The cube face located at the image plane of the phase plate was covered with a white spray to make it reflective. The same vibrometry parameters were used. A longer ultrasound burst of 10 cycles was transmitted instead of 5 cycles as well. A picture of the setup is depicted in Fig. S8B. A block with no engraving was also measured with the same setup (Fig. 3F) as a control. To produce the desired wavefront at the image plane, we employed the Iterative Angular Spectrum Approach (IASA) to calculate the relative phase shifts across the phase plate pixels, following the method described in Ref. (*10*). Because the phase plate was positioned 4 mm from the transducer, the acoustic field—assumed to have a uniform phase at the transducer surface—was first numerically propagated to the phase plate location. The required phase distribution for the plate design was then obtained by iteratively propagating the wave between the image plane and the phase plate plane, applying amplitude constraints at each step in both planes. The IASA-computed phase distribution was then converted to a height for each pixel using the equation $h = \frac{\Delta\phi}{2\pi f_0} \times \frac{v_0 v_x^{\text{eff}}}{(v_0 - v_x^{\text{eff}})}$ where $\Delta\phi$ is the phase shift for one pixel. Finally, this phase plate was filled with a 3D point cloud for engraving. As for the two-foci hologram along the propagation direction, a simpler version was used. Two spherical waves were numerically back-propagated from the two-foci positions, and their fields were added. The obtained phase was

Table 1: **Attenuation of different materials** Attenuation for water, soft tissue (*31*), BK7 glass and steel (*22*), silicone (*20*) and VeroClear (*19*), a photopolymer traditionally used for 3D printed phase plates.

	Water	BK7 glass	A36 steel	Soft tissue	VeroClear	Silicone
Attenuation ($\mathrm{dB\,MHz^{-1}\,cm^{-1}}$)	0.0022	0.05	0.124	0.75	3.7	4

Table 2: **Effective properties of the engraved area (metamaterial)** Density, longitudinal speed of sound, and attenuation of the bulk medium (BK7 glass) and the engraved area, treated as an effective medium.

	Bulk medium	Effective medium		
		X	Y	Z
Density	$\rho_0 = 2525\ \mathrm{kg\,m^{-3}}$	$1.21\rho_0$	ρ_0	ρ_0
Longitudinal speed of sound	$v_0 = 5816\ \mathrm{m\,s^{-1}}$	$0.83v_0$	v_0	v_0
Attenuation	$\alpha = 3.3\ \mathrm{dB\,MHz^{-1}\,m^{-1}}$	1.1α	1.3α	1.2α

then used similarly for the design of the phase plate.

Stacking of samples for modularity

Different combinations of glass blocks were stacked (Fig. 4). We 3D printed a simple scaffold to align the stacked glass blocks. A thin layer of water was used for coupling the blocks, and two screws applied a light pressure between the blocks to reduce the acoustic reflection between the interfaces efficiently. Three scans were then performed with the vibrometer to cover the assembly (Fig. S6).

Statistics

For all line plots, the distribution is depicted as follows: mean values were individually plotted, whiskers show ± standard deviation. Values are presented as “mean value ± standard deviation” unless specified.

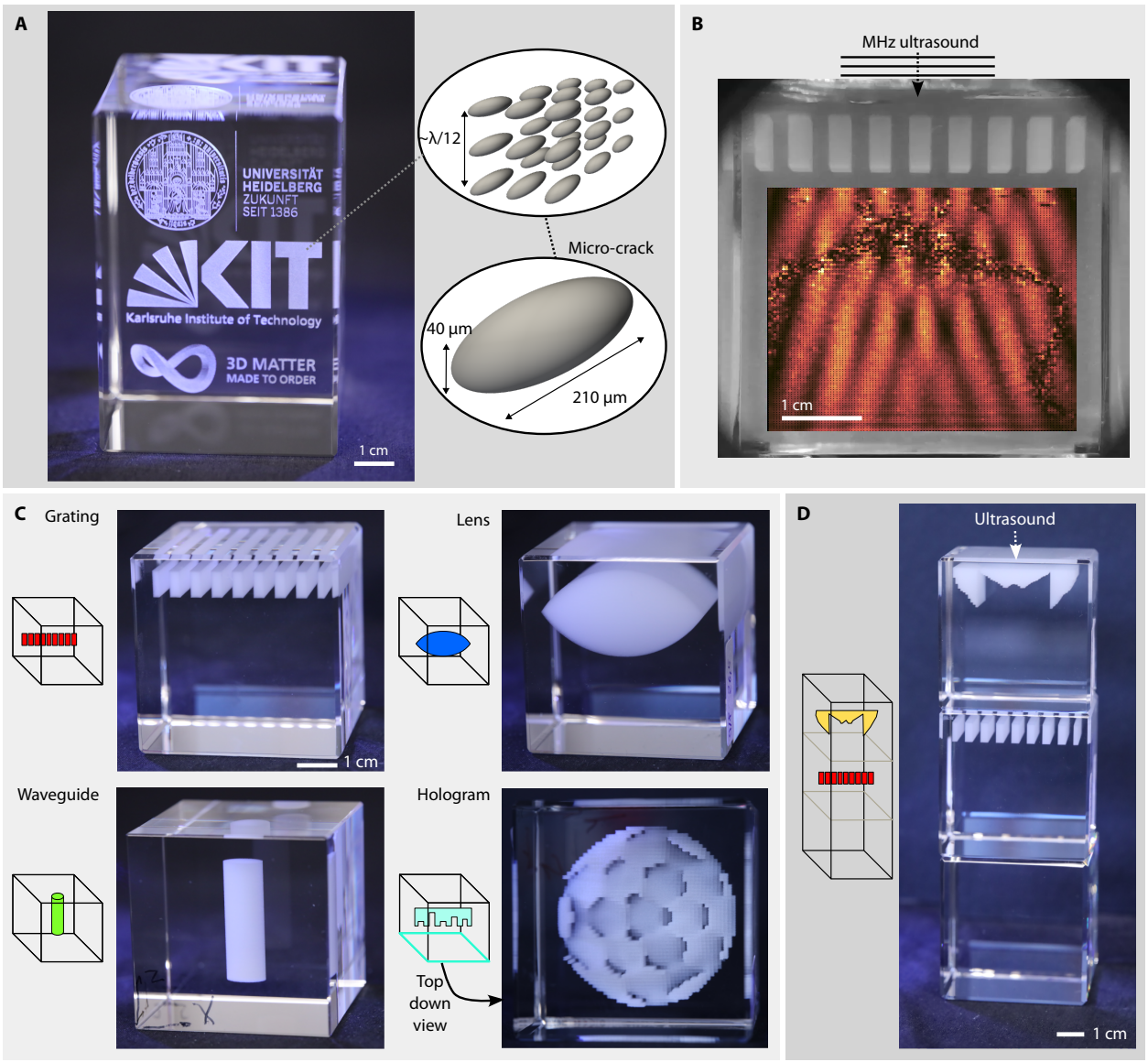


Figure 1: **Overview of a MHz ultrasound metamaterial in glass with subsurface laser engraving.** (**A**) Photograph of a laser-engraved glass sample. A close-up shows a schematic of a pattern of individual microcracks. (**B**) An ultrasonic wavefront can be shaped at MHz frequencies. An experimental grating inside a 5 cm glass cube is provided. (**C**) Several patterns can be engraved in 3D and make blocks with different acoustic properties. A lens, a waveguide, a grating, and a hologram will be studied. (**D**) Engraved blocks can be stacked, providing modularity and even more acoustic properties. All scale bars indicate 1 cm.

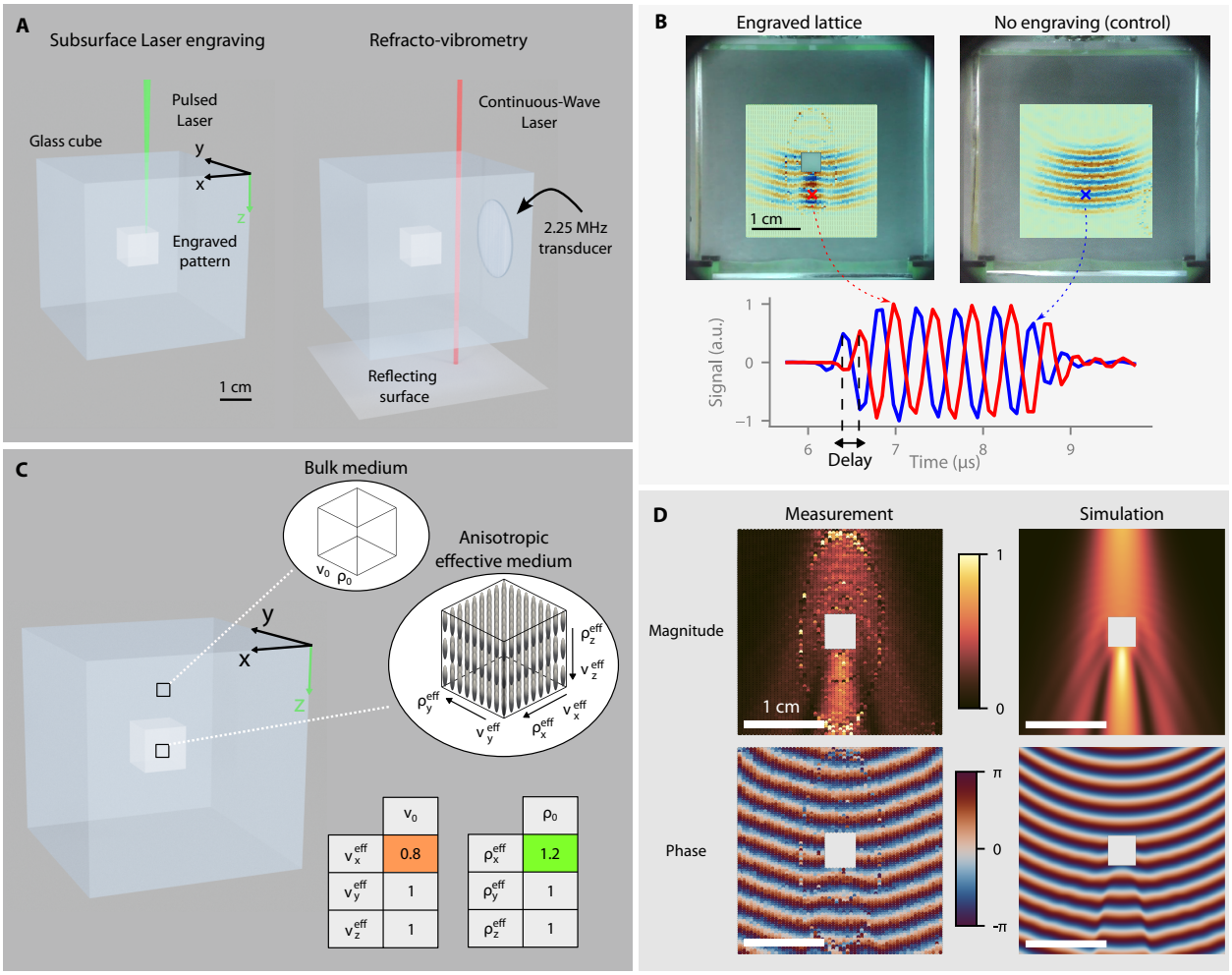


Figure 2: **Effective medium characterization.** (**A**) Schematics of the subsurface laser engraving process (left) and of the refracto-vibrometry measurements (right). The z axis is chosen as the engraving direction of the laser and depicted in green. (**B**) Refracto-vibrometry measurements show that a 5-cycle burst at 2.25 MHz is delayed when propagating through an engraved voxel compared to a control block (without any engraving). (**C**) With the time-of-flight calculations, the effective speed of sound was determined in the engraved area for every propagation direction. From the effective speed of sound, the effective density was retrieved. (**D**) T-matrix simulations show a good agreement with the refracto-vibrometry measurements. All scale bars indicate 1 cm.

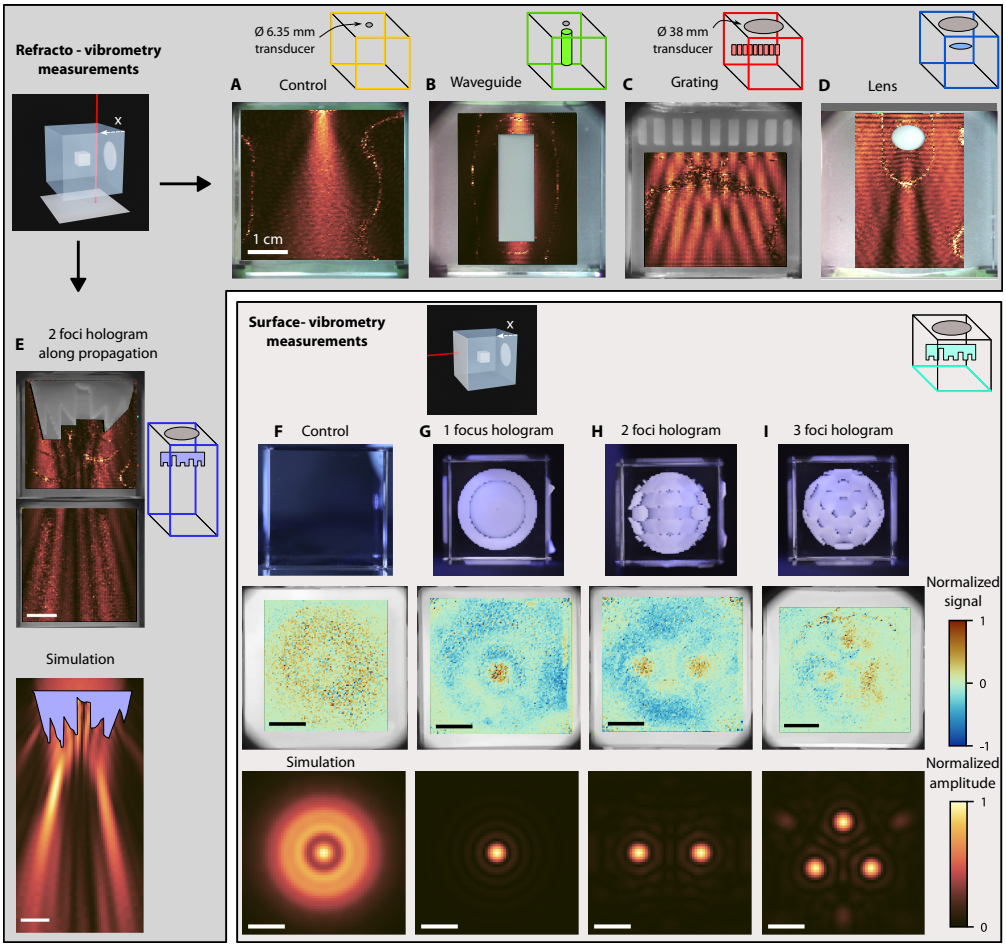


Figure 3: **Element library.** Different blocks were made to control the wavefront inside the glass. An ultrasound signal was transmitted along the x direction. **A** to **E** were measured with a refracto-vibrometry technique revealing: (**A**) a control block without any engraving, (**B**) a waveguide, (**C**) a grating, (**D**) a biconvex converging lens, and (**E**) a hologram with two foci. For (**E**), a simulation is also provided for comparison. **F** to **I** were measured with a standard surface vibrometry technique, revealing: (**F**) a control block, (**G**) a one-focus hologram, (**H**) a two-foci hologram, (**I**) a three-foci hologram whose image plane coincides with a face of the cube opposite the transducer. For **F** to **I**, top-down photographs of the samples are provided (top), as well as the vibrometry time signal (middle), and simulations (bottom) for comparison. For all the blocks, a schematic of the setup is depicted. The cube's face, which had been measured, is highlighted in color. For the refracto-vibrometry, a 3D sound field is reduced to a 2D projection. Two opposite faces are highlighted to depict the measurement direction. All scale bars indicate 1 cm.

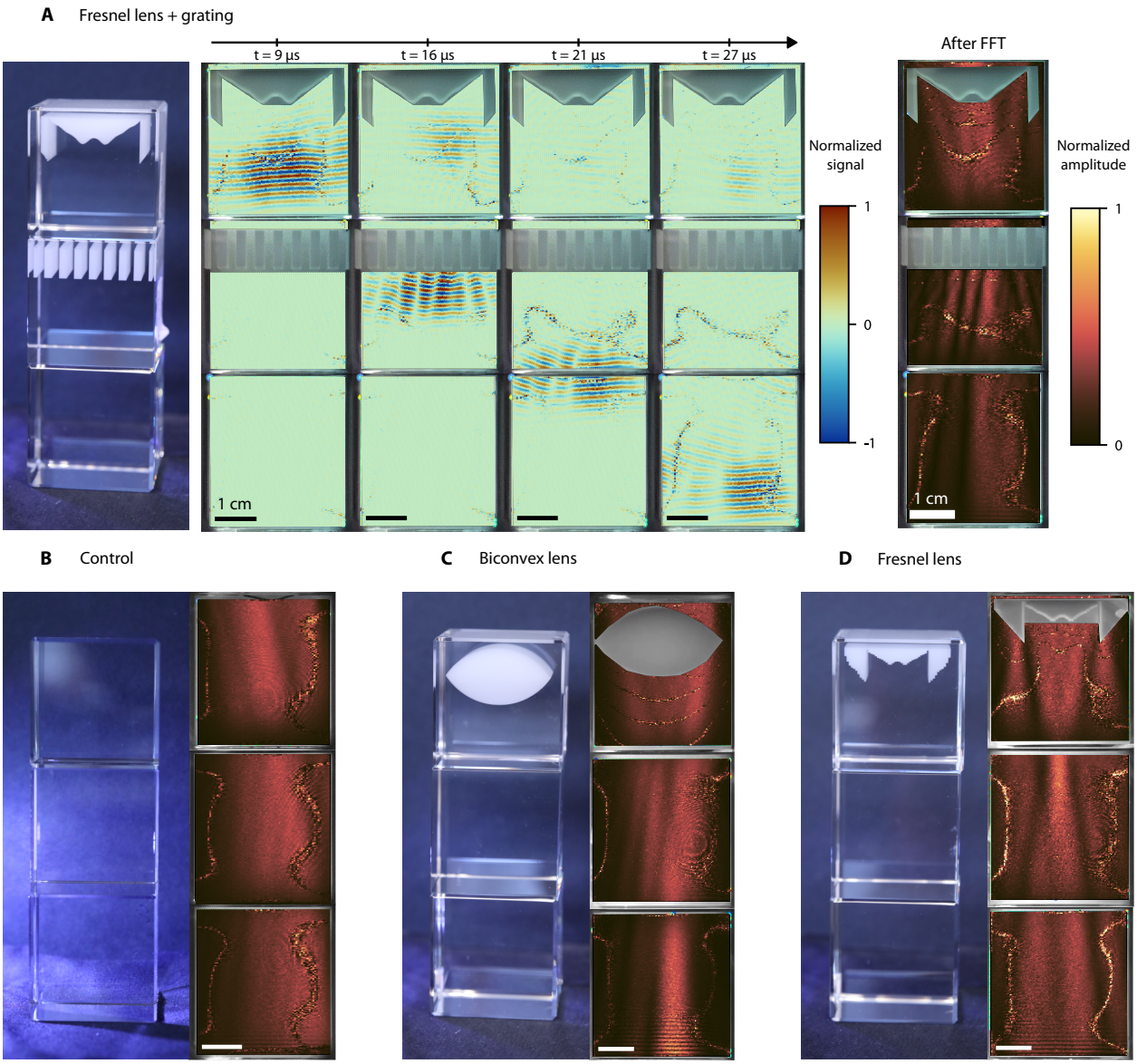


Figure 4: **Stacking of blocks for modularity.** (**A**) Picture of the assembly of a converging Fresnel lens and a grating. The vibrometry signal shows the propagation of the field with limited reflection between the blocks. After the Fast Fourier Transform, the converging effect as well as the grating are visible. (**B**)-(**D**) Picture and Fourier transform of the vibrometry signal for (**B**) a control assembly (without any engraving), (**C**) biconvex converging lens, and (**D**) converging Fresnel lens. All scale bars indicate 1 cm.

References and Notes

1. D. Attali, *et al.*, Deep transcranial ultrasound stimulation using personalized acoustic metamaterials improves treatment-resistant depression in humans. *Brain Stimulation* **18**, 1004–1014 (2025).

2. C. Cengiz, *et al.*, A Roadmap to Holographic Focused Ultrasound Approaches for Generating Gradient Thermal Patterns. *Int. J. Numer. Methods Biomed. Eng.* **41**, e70055 (2025).

3. M. Xu, *et al.*, Micro-Acoustic Holograms for Detachable Microfluidic Devices. *Small* **20**, 2307529 (2024).

4. M. Shi, P. Fischer, K. Melde, Acoustic holographic assembly of cell-dense tissue constructs. *Biofabrication* **17**, 035009 (2025).

5. M. Derayatifar, M. Habibi, R. Bhat, M. Packirisamy, Holographic direct sound printing. *Nat. Commun.* **15**, 6691 (2024).

6. H. Zhao, *et al.*, Nondestructive Evaluation of Special Defects Based on Ultrasound Metasurface. *Front. Mater.* **8**, 802001 (2022).

7. P. Kruizinga, *et al.*, Compressive 3D ultrasound imaging using a single sensor. *Sci. Adv.* **3**, e1701423 (2017).

8. J. Lee, Y. Y. Kim, Anisotropic elastic metamaterials for novel wave manipulation: a review. *Eur. J. Mech. A Solids* **113**, 105696 (2025).

9. T. W. Hughes, I. A. D. Williamson, M. Minkov, S. Fan, Wave physics as an analog recurrent neural network. *Sci. Adv.* **5**, eaay6946 (2019).

10. K. Melde, A. G. Mark, T. Qiu, P. Fischer, Holograms for acoustics. *Nature* **537**, 518–522 (2016).

11. R. Burstow, *et al.*, Acoustic holography in biomedical applications. *Phys. Med. Biol.* **70**, 06TR01 (2025).

12. M. D. Brown, B. T. Cox, B. E. Treeby, Binary Volume Acoustic Holograms. *Phys. Rev. Appl.* **19**, 044032 (2023).

13. C. J. Naify, A. Titovich, M. R. Haberman, What is an acoustic metamaterial? *Proc. Mtgs. Acoust.* **51**, 065002 (2023).

14. S. Qu, *et al.*, Underwater metamaterial absorber with impedance-matched composite. *Sci. Adv.* **8**, eabm4206 (2022).

15. R.-M. Guillermic, M. Lanoy, A. Strybulevych, J. H. Page, A PDMS-based broadband acoustic impedance matched material for underwater applications. *Ultrasonics* **94**, 152–157 (2019).

16. B. Assouar, *et al.*, Acoustic metasurfaces. *Nat. Rev. Mater.* **3**, 460–472 (2018).

17. Y. Jin, R. Kumar, O. Poncelet, O. Mondain-Monval, T. Brunet, Flat acoustics with soft gradient-index metasurfaces. *Nat. Commun.* **10**, 143 (2019).

18. M. Xu, W. S. Harley, Z. Ma, P. V. S. Lee, D. J. Collins, Sound-Speed Modifying Acoustic Metasurfaces for Acoustic Holography. *Adv. Mater.* **35**, 2208002 (2023).

19. M. Bakaric, *et al.*, Measurement of the ultrasound attenuation and dispersion in 3D-printed photopolymer materials from 1 to 3.5 MHz. *J. Acoust. Soc. Am.* **150**, 2798–2805 (2021).

20. K. Itsumi, Y. Hosono, N. Yamamoto, Y. J. Yamashita, Low acoustic attenuation silicone rubber lens for medical ultrasonic array probe. *IEEE Trans. Ultrason. Ferroelectr. Freq. Control* **56**, 870–874 (2009).

21. D. Andrés, *et al.*, Holographic Focused Ultrasound Hyperthermia System for Uniform Simultaneous Thermal Exposure of Multiple Tumor Spheroids. *Cancers* **15**, 2540 (2023).

22. K. Ono, A Comprehensive Report on Ultrasonic Attenuation of Engineering Materials, Including Metals, Ceramics, Polymers, Fiber-Reinforced Composites, Wood, and Rocks. *Applied Sciences* **10**, 2230 (2020).

23. J. Szelazek, paper at the 11th European Conference on Non-Destructive Testing, Prague, 6–10 October 2014.

24. P. C. Waterman, New Formulation of Acoustic Scattering. *J. Acoust. Soc. Am.* **45**, 1417–1429 (1969).

25. N. Ustimenko, C. Rockstuhl, A. V. Kildishev, Optimal multipole center for subwavelength acoustic scatterers. *Appl. Phys. Lett.* **126**, 142201 (2025).

26. N. Ustimenko, A. B. Evlyukhin, V. Kyrimi, A. V. Kildishev, C. Rockstuhl, Lattice-induced sound trapping in biperiodic metasurfaces of acoustic resonators. *preprint* (2025), doi:arXiv. 2510.17750.

27. J. A. I. Martínez, M. Farhat, Y. Wu, A. Khelif, Ultrasound underwater coherent perfect absorbers. *Phys. Rev. Appl.* **23**, 054023 (2025).

28. R. Sun, J. Lem, Y. Kai, W. DeLima, C. M. Portela, Tailored ultrasound propagation in microscale metamaterials via inertia design. *Sci. Adv.* **10**, eadq6425 (2024).

29. M. Bakhtiari-Nejad, A. Elnahhas, M. R. Hajj, S. Shahab, Acoustic holograms in contactless ultrasonic power transfer systems: Modeling and experiment. *J. Appl. Phys.* **124**, 244901 (2018).

30. Materials and methods are available as supplementary material.

31. H. Shankar, P. S. Pagel, D. S. Warner, Potential Adverse Ultrasound-related Biological Effects: A Critical Review. *Anesthesiology* **115**, 1109–1124 (2011).

32. L. Zipser, H. Franke, paper presented at the 2007 IEEE Ultrasonics Symposium, New York, NY, 28-31 October 2007.

33. A. Wood, *A Textbook of Sound* (Macmillan, NY, 1941).

34. D. Torrent, J. Sánchez-Dehesa, Effective parameters of clusters of cylinders embedded in a nonviscous fluid or gas. *Phys. Rev. B* **74**, 224305 (2006).

35. S. Giordano, Effective medium theory for dispersions of dielectric ellipsoids. *J. Electrostat.* **58**, 59–76 (2003).

36. M. Smagin, I. Toftul, K. Y. Bliokh, M. Petrov, Acoustic lateral recoil force and stable lift of anisotropic particles. *Phys. Rev. Appl.* **22**, 064041 (2024).

37. I. D. Toftul, K. Y. Bliokh, M. I. Petrov, F. Nori, Acoustic Radiation Force and Torque on Small Particles as Measures of the Canonical Momentum and Spin Densities. *Phys. Rev. Lett.* **123**, 183901 (2019).

38. A. Rahimzadegan, *et al.*, A Comprehensive Multipolar Theory for Periodic Metasurfaces. *Adv. Opt. Mater.* **10**, 2102059 (2022).

39. S. Stein, Addition Theorems for Spherical Wave Functions. *Q. Appl. Math.* **19**, 15–24 (1961).

40. D. Beutel, I. Fernandez-Corbaton, C. Rockstuhl, Unified lattice sums accommodating multiple sublattices for solutions of the Helmholtz equation in two and three dimensions. *Phys. Rev. A* **107**, 013508 (2023).

41. D. Beutel, I. Fernandez-Corbaton, C. Rockstuhl, treams – a T-matrix-based scattering code for nanophotonics. *Comput. Phys. Commun.* **297**, 109076 (2024).

42. O. Svelto, *Principles of Lasers* (Springer, NY, 2010).

43. M. Abramowitz, I. A. Stegun, *Handbook of Mathematical Functions: With Formulas, Graphs, and Mathematical Tables* (Dover Publications, 1965).

44. F. I. Ulu, R. Mohan, R. P. S. Tomar, paper presented at the ASME 2019 International Mechanical Engineering Congress and Exposition, Salt Lake City, UT, 11-14 November 2019.

45. J. Vaithilingam, E. Saleh, R. D. Wildman, R. J. M. Hague, C. J. Tuck, Optimisation of Substrate Angles for Multi-material and Multi-functional Inkjet Printing. *Sci. Rep.* **8**, 9030 (2018).

46. L. Su, Y. Chen, A. Y. Yi, F. Klocke, G. Pongs, Refractive index variation in compression molding of precision glass optical components. *Appl. Opt.* **47**, 1662–1667 (2008).

Acknowledgments: We thank Dr. Jochen Schell from Polytec company for accompanying us on the manipulation of the PSV-500 and for his expertise on refracto-vibrometry measurements. We also thank Mr. Holger Hartmann from M+B Lasertechnik GmbH for his expertise on the

laser engraving of glass samples, Dr. Kai Melde for the borrowed transducers, and Setthibhak Suthithanakom for his help with the design of the 3D-printed scaffold to stack glass blocks.

Funding: This work was supported by the Deutsche Forschungsgemeinschaft (DFG, German Research Foundation) under Germany's Excellence Strategy via the Excellence Cluster 3D Matter Made to Order and from the Carl Zeiss Foundation via CZF-Focus@HEiKA.

Author contributions: Conceptualization: OD, AGA, CR, PF
Methodology: OD, NU, AGA, CR, PF
Investigation: OD, NU, AGA, LG
Visualization: OD, NU
Resources: PF
Supervision: AGA, CR, PF
Writing—original draft: OD, NU
Writing—review & editing: OD, NU, AGA, LG, CR, PF

Competing interests: All authors declare they have no competing interests.

Data and materials availability: All data needed to evaluate the conclusions in the paper are present in the paper and/or the Supplementary Materials.

Supplementary materials

Materials and Methods
Figs. S1 to S11
Tables S1 to S2
References *(32-46)*

Supplementary Materials for

Ultrasonic metamaterial at MHz frequencies using microstructured glass

Oscar Demeulenaere*, Nikita Ustimenko, Athanasios Athanassiadis

Lovish Gulati, Carsten Rockstuhl, Peer Fischer

*Corresponding author. Email: oscar.demeulenaere@mr.mpg.de

This PDF file includes:

Materials and Methods

Figures S1 to S11

Tables S1 to S2

Materials and Methods

Refracto-vibrometry measurements

As explained in Ref. (*32*), refracto-vibrometry can be used in transparent solids. With refracto-vibrometry, a 3D sound field is reduced to a 2D projection. To verify that this projection did not interfere with our time-of-flight measurements, we also measured the speed of sound in the bulk medium with a pulser receiver, see Fig. S7.

The refracto-vibrometry setup was composed of a Polytec Scanning Vibrometer PSV-500, a signal generator, an amplifier, and an ultrasound transducer. The acquisition parameters are described in Table S2. We placed the glass cube inside a 3D printed base and placed a reflective surface behind it. A picture of the setup is given in Fig. S8. We calibrated the position between the scan points from the distance on camera of one edge of the glass cube. To focus the laser spot, we removed the glass cube and moved the reflective surface to the middle plane of the glass cube. The laser spot was then sharp inside the glass cube, but a bit bigger on the reflective screen, back to its original position behind the cube. The refracto-vibrometry time-domain signal for each scanning point was then exported as a uff file. The raw data was imported and analyzed with the Fast Fourier Transform (FFT) using Python 3.12.

Measurement of the effective speed of sound and density with refracto-vibrometry

For the measurement of the effective speed of sound, two samples were used: a control block and a block with an engraved voxel at the center, see Fig. S9. Both blocks were positioned inside a 3D printed base to ensure the positions of the scanning points are identical in both measurements. We then used an Olympus transducer with a diameter of 6.35 mm and a center frequency of $f_0 = 2.25$ MHz. A 5-cycle burst was transmitted at f_0. From the refracto-vibrometry data, we measured the time-of-flight between two scanning points with a fixed distance d between them. We measured t_1^{C} and t_2^{C} for the control block and t_1^{E} and t_2^{E} for the engraved block (Fig. S9). The effective speed of sound was then calculated as $v_i^{\mathrm{ref}} = \left(\frac{t_2^{\mathrm{E}} - t_1^{\mathrm{E}} + t_2^{\mathrm{C}} - t_1^{\mathrm{C}}}{h} + \frac{1}{v_0}\right)^{-1}$ where ρ_0 and v_0 are the density and speed of sound of the bulk medium and h is the height of the engraved voxel along the propagation direction of the ultrasound beam. To calculate the effective density, we used the equation $\rho_i^{\mathrm{eff}} = \frac{\rho_0 v_0}{v_i^{\mathrm{ref}}} \times \frac{1+r_i}{1-r_i}$ where the pressure reflection coefficient r was found very small

compared to 1, so that we could set $r_i \approx 0$ and find the effective density simply as $\rho_i^{\text{eff}} = \frac{\rho_0 v_0}{v_i^{\text{ref}}}$. This procedure was repeated for every propagation directions ($i = x, y, z$).

However, with the refracto-vibrometry measurements, a 3D sound field is reduced to a 2D projection. Therefore, the size of the engraved voxel along the vibrometry laser relative to the block size affects the measured signal and consequently the effective properties. Therefore, to calculate them, we considered an engraved voxel that was large enough along the refracto-vibrometry laser direction (Fig. S2).

Measurement of the effective speed of sound for different frequencies

A similar setup as above was used to measure the effect of frequency on the properties of the engraved area. The same control and engraved samples were used along with three transducers whose frequencies were 0.5, 2.25, and 5 MHz, respectively (Fig. S4). A Fast-Fourier-Transform (FFT) was computed from the refracto-vibrometry data. We selected a scan point below the engraving area. From the signal at each frequency f, we measured the phase shift $\Delta\phi$ between the signal from the incident field s_1^{E} (control sample) and the field propagated through the engraved voxel s_1^{C} (engraved sample). The phase shift was then calculated as $\Delta\phi = arg(\frac{s_1^{\text{E}}}{s_1^{\text{C}}})$ and the effective speed of sound as $v_i^{\text{ref}} = \left(\frac{\Delta\phi}{2\pi f h} + \frac{1}{v_0}\right)^{-1}$ where v_0 is the speed of sound of the bulk medium and h is the height of the engraved voxel along the propagation direction of the ultrasound beam. This procedure was performed only for the x axis ($i = x$).

T-matrix method for simulating the microcrack arrays

Below we present a theoretical description of the acoustic response of the microcrack metamaterial sketched in Fig. S10. We assume that the microcracks are identical and consider each microcrack as an anisotropic ellipsoid of semiaxes $a_x = 19.7$ μm, $a_y = 19.45$ μm, and $a_z = 105.5$ μm along the x, y, and z directions, respectively, which yield the microcrack volume $V_{\text{e}} = \frac{4\pi}{3}abc$. We also assume that the principal axes of the microcrack material coincide with the Cartesian coordinate axes. Then, the microcrack has the density components $\{\rho_x, \rho_y, \rho_z\}$ and the bulk modulus K, while the isotropic background medium has the density $\rho_0 = 2525$ kg m^{-3}, speed of sound $v_0 = 5816$ m s^{-1}, and bulk modulus $K_0 = \rho_0 v_0^2 \approx 85.41$ GPa at frequency $f_0 = 2.25$ MHz (Table 1). Although

the background medium has a nonzero shear modulus, the shear waves are neglected because they cannot be excited by a normally incident pressure (acoustic) wave. The attenuation in the background is also neglected. Therefore, we can treat the bulk glass medium as a non-viscous fluid.

Estimation of the microcrack material parameters through the effective medium theory

To find K, we apply Wood's law (*33, 34*)

$$\frac{1}{\widetilde{K}^{\text{eff}}} = \frac{\eta}{\widetilde{K}} + (1-\eta)\,, \tag{S1}$$

where the bulk moduli have been normalized by K_0, and the fraction of the microcrack volume to the unit cell volume is $\eta \approx 0.077$.

To find ρ_i, we adopt the approach developed for a diluted ($\eta \ll 1$) ensemble of electromagnetic ellipsoidally-shaped scatterers (*35*). Let a uniform velocity field $\mathbf{u}_0$ be applied to the ellipsoidal microcrack. Then, the field inside the microcrack is also uniform, and its components are given by $u_{ix} = \frac{u_{0x}}{\widetilde{\rho}_x + L_x(1-\widetilde{\rho}_x)}$, $u_{iy} = \frac{u_{0y}}{\widetilde{\rho}_y + L_y\left(1-\widetilde{\rho}_y\right)}$, and $u_{iz} = \frac{u_{0z}}{\widetilde{\rho}_z + L_z(1-\widetilde{\rho}_z)}$, where the densities have been normalized by ρ_0, and the depolarization factors of the considered ellipsoidal microcrack have been computed $L_x = 0.472$, $L_y = 0.478$, and $L_z = 0.05$ (*36*). Next, because the array size is larger along the laser direction than its sizes in the transverse cross section, the volume-averaged effective field $\mathbf{u}^{\text{eff}} = \eta\mathbf{u}_i + (1-\eta)\mathbf{u}_0$ can be approximated by the field generated by a large ellipsoid of the same shape, so that $u_x^{\text{eff}} = \frac{u_{0x}}{\widetilde{\rho}_x^{\text{eff}} + L_x\left(1-\widetilde{\rho}_x^{\text{eff}}\right)}$, $u_y^{\text{eff}} = \frac{u_{0y}}{\widetilde{\rho}_y^{\text{eff}} + L_y\left(1-\widetilde{\rho}_y^{\text{eff}}\right)}$, and $u_z^{\text{eff}} = \frac{u_{0z}}{\widetilde{\rho}_z^{\text{eff}} + L_z\left(1-\widetilde{\rho}_z^{\text{eff}}\right)}$. Hence, the components of the effective density tensor can be calculated as follows

$$\left[\widetilde{\rho}_i^{\text{eff}}\right]^{-1} = 1 + \frac{\eta\left(\left[\widetilde{\rho}_i\right]^{-1} - 1\right)}{1 + (1-\eta)L_i\left(\left[\widetilde{\rho}_i\right]^{-1} - 1\right)}\,. \tag{S2}$$

As the effective densities of the microcrack array, we take the following values $\widetilde{\rho}_x^{\text{eff}} = 1.21$, and $\widetilde{\rho}_y^{\text{eff}} = \widetilde{\rho}_z^{\text{eff}} = 1$ (Table 2). To calculate the effective bulk modulus, we take the normalized speed of sound $\widetilde{v}_x^{\text{eff}} \equiv v_x^{\text{eff}}/v_0 = 0.83$ (Table 2) and calculate $\widetilde{K}^{\text{eff}} = \widetilde{\rho}_x^{\text{eff}}(\widetilde{v}_x^{\text{eff}})^2 \approx 0.83$ corresponding to the x direction ($\widetilde{K}^{\text{eff}} \equiv 1$ along y and z). If we plug $\widetilde{K}^{\text{eff}}$ and $\widetilde{\rho}_i^{\text{eff}}$ into Eqs. (S1) and (S2), respectively, we obtain the normalized material parameters of the microcrack $\widetilde{K} = 0.28$, $\widetilde{\rho}_x = -7.42$, and $\widetilde{\rho}_y = \widetilde{\rho}_z = 1.00$. To calculate the normalized compressibility of the microcrack, we average the inverse bulk modulus over the propagation directions, so that $\widetilde{\beta} = \left(\widetilde{K}^{-1} + 2\right)/3 \approx 1.86$ where $\beta_0 = K_0^{-1}$.

Response of a microcrack in the quasistatic approximation

Since the wavelength in the bulk glass medium $\lambda = v_0/f_0 \approx 2.58$ mm at $f_0 = 2.25$ MHz is much larger than the microcrack ($c \sim 0.1$ mm), we simulate the microcrack response in the quasistatic approximation, when the monopole and dipole polarizabilities of an ellipsoidally-shaped microcrack read as (*36*)

$$(\alpha_{\rm M})^{-1} = \left(\alpha_{\rm M}^{\rm st}\right)^{-1} - \frac{{\rm i}k^3}{4\pi}\,, \quad \text{and} \quad (\boldsymbol{\alpha}_{\rm D})^{-1} = \left(\boldsymbol{\alpha}_{\rm D}^{\rm st}\right)^{-1} - \frac{{\rm i}k^3}{12\pi}\mathbf{I}_3\,, \tag{S3}$$

where $k = 2\pi/\lambda$, and $\mathbf{I}_n$ is the $n\times n$ identity matrix. The static monopole and dipole polarizabilities of an anisotropic ellipsoid are the following functions of the normalized compressibility $\widetilde{\beta} \equiv \beta/\beta_0$ and density $\widetilde{\rho}_i \equiv \rho_i/\rho_0$, respectively,

$$\alpha_{\rm M}^{\rm st} = V_{\rm e}\left(\widetilde{\beta} - 1\right)\,, \quad \text{and} \quad \left(\alpha_{\rm D}^{\rm st}\right)_i = V_{\rm e}\frac{\widetilde{\rho}_i - 1}{\widetilde{\rho}_i + L_i\,(1-\widetilde{\rho}_i)}\,, \quad i = x, y, z\,. \tag{S4}$$

The polarizabilities (S3) determine the acoustic T-matrix of the standalone microcrack in the monopole-dipole approximation at frequency f_0 as (*37*)

$$\mathbf{T} = \begin{pmatrix} {\rm T}_{\rm M} & \mathbf{0} \\ \mathbf{0} & \mathbf{T}_{\rm D} \end{pmatrix} = \frac{{\rm i}k^3}{12\pi}\begin{pmatrix} 3\alpha_{\rm M} & \mathbf{0} \\ \mathbf{0} & \mathbf{F}^{-1}\boldsymbol{\alpha}_{\rm D}\mathbf{F} \end{pmatrix}, \tag{S5}$$

where matrices $\mathbf{F}$ and $\mathbf{F}^{-1}$ convert the Cartesian components of the dipole moment to those in the spherical harmonics basis and vice versa, respectively, (*38*)

$$\mathbf{F} = \frac{1}{\sqrt{2}}\begin{pmatrix} 1 & 0 & -1 \\ -{\rm i} & 0 & -{\rm i} \\ 0 & \sqrt{2} & 0 \end{pmatrix}, \quad \text{and} \quad \mathbf{F}^{-1} = \frac{1}{\sqrt{2}}\begin{pmatrix} 1 & {\rm i} & 0 \\ 0 & 0 & \sqrt{2} \\ -1 & {\rm i} & 0 \end{pmatrix}. \tag{S6}$$

Multiple scattering formalism

As T-matrix (S5) is known, we can consider a finite array of $N \equiv N_x \times N_y \times N_z$ microcracks with spacing $s_x = 90$ μm, $s_y = 90$ μm, and $s_y = 270$ μm between the microcracks; hence, the array size along the axis $i = x, y, z$ is $d_i = (N_i - 1)s_i + 2a_i$. Note that (S1) and (S2) do not consider interactions between the microcracks; hence, (S5) is the T-matrix of the standalone microcrack. In the following, we consider two coordinate systems, the first one (x, y, z) is associated with the microcrack pattern, while the second one (x', y', z') is always fixed and given by a permutation of (x, y, z). In contrast to Fig. S2, an incident wave in our T-matrix code always propagates along

the $(-x')$ direction. In Fig. S2, $d_{x'}$ always corresponds to $N_{x'} = N_{y'} = 45$ microcracks, while $d \equiv d_{z'} \propto N_{z'}$ varies. Note also that in Fig. S9, the thickness along the x' axis is denoted as $h \equiv d_{x'}$.

The T-matrix method allows for the accommodation of mutual acoustic interaction between microcracks through the analytically known translation coefficients of spherical waves (*39*). Note that within the T-matrix method, we can model the acoustic response of an array that has a finite number of scatterers along all the directions (*25*); however, for a relatively high N, it becomes computationally demanding, if not impossible, since we need to invert a matrix of order $4N$. Therefore, to simplify and speed up the calculations, we assume periodic boundary conditions along the refracto-vibrometry direction (the z' axis) with the period of microcracks $s_{z'}$, *i.e.*, $N_{z'} \to \infty$. In this case, the 3D scattering problem becomes a 2D one, and the mutual interaction of the infinite number of microcracks can be considered by means of the lattice sums [see Eq. (D6) in Ref. (*26*)], which can be computed fast in *acoustotreams*, v.0.2.5. Then, only the following 4×4 matrix should be inverted to obtain the T-matrix of a microcrack chain in the spherical wave basis under the monopole-dipole approximation

$$\mathbf{T}_{\text{chain}} = \left(\mathbf{I}_4 - \mathbf{\Sigma}\mathbf{T}\right)^{-1} \mathbf{T}\,, \tag{S7}$$

where $\mathbf{\Sigma} = 2\sqrt{\pi} D_{3,0,0}\mathbf{I}_4 + \sqrt{5\pi} D_{3,2,0}\mathbf{\Xi}$, $\mathbf{\Xi} = \text{diag}\,[0; 2/5; -1; 2/5]$, and the sums $D_{3,\ell,m}$ are defined by Eq. (1) in Ref. (*40*) for one-dimensional lattices, with $\mathbf{k}_{\parallel} = \mathbf{0}$ (normal incidence) and $\mathbf{r} = \mathbf{0}$. Next, we transform (S7) in the spherical wave basis into the following 3×3 matrix in the cylindrical wave basis using the same approach as in (*41*) but for the scalar waves. For the chain period $s_{z'} < \lambda$ and normal incidence, one can show that the transformation is given by

$$\mathcal{T}_{\text{chain}} = \frac{\lambda}{2 s_{z'}} \mathbf{U}\mathbf{T}_{\text{chain}}\mathbf{V}\,, \tag{S8}$$

with the matrices

$$\mathbf{U} = \frac{1}{\sqrt{2}} \begin{pmatrix} 0 & -\sqrt{3} & 0 & 0 \\ \sqrt{2} & 0 & 0 & 0 \\ 0 & 0 & 0 & -\sqrt{3} \end{pmatrix}, \quad \text{and} \quad \mathbf{V} = \frac{1}{\sqrt{2}} \begin{pmatrix} 0 & \sqrt{2} & 0 \\ -\sqrt{3} & 0 & 0 \\ 0 & 0 & 0 \\ 0 & 0 & -\sqrt{3} \end{pmatrix}. \tag{S9}$$

Now we can consider a finite array of $N_{x'} \times N_{y'}$ infinite chains, extended along the z' axis. Assume that the coordinates of the chains in the $x'y'$ plane are given by vectors $\mathbf{r}'_{ij} = (x'_i, y'_j, 0)$

with $x'_i = \left(i - \frac{N_{x'}+1}{2}\right) s_{x'}$ and $y'_j = \left(j - \frac{N_{y'}+1}{2}\right) s_{y'}$ where $1 \leq i \leq N_{x'}$ and $1 \leq j \leq N_{y'}$. $N_{x'}$ and $N_{y'}$ are odd natural numbers. As a driving field we consider a Gaussian beam integrated along the z' axis from $z' = -L$ to $z' = L$, where L is the size of the cube, *i.e.*, the incident field is $p_{\text{inc}}(x', y') \approx p_0(x', y')\mathrm{e}^{-\mathrm{i}kx'}$ where $p_0(x', y') = \frac{\sqrt{\pi}W_{x'}}{L}\mathrm{erf}\left(\frac{L}{2W_{x'}}\right)\frac{w_{x'_0}}{w_{x'}}\exp\left(-\frac{y'^2}{W_{x'}^2} + \mathrm{i}\psi_{x'}\right)$ accounts for the averaging of the beam along the laser direction z', $\mathrm{erf}(...)$ is the error function, the complex-valued beam width is $W_{x'} = w_{x'}\left(1 + \mathrm{i}\frac{kw_{x'}^2}{2R_{x'}}\right)^{-1/2}$, the real-valued beam width is $w_{x'} = w_{x'_0}\sqrt{1 + \frac{(x'-x'_0)^2}{l_R^2}}$, the radius of curvature is $R_{x'} = (x' - x'_0)\left[1 + \frac{l_R^2}{(x'-x'_0)^2}\right]$, the Gouy phase is $\psi_{x'} = \arctan\left[\frac{x'-x'_0}{l_R}\right]$, and the Rayleigh length is $l_R = \pi w_0^2/\lambda$ for waist radius $w_{x'_0} = 3.175$ mm at the upper face of the cube $x'_0 = L/2$ mm (*42*). We can approximately write the desired total pressure field as

$$\boxed{p(x', y') \approx p_0(x', y') \times \left[\mathrm{e}^{-\mathrm{i}kx'} + \xi\left(d_{z'}\right) p_{\text{sca}}(x', y')\right]}, \tag{S10}$$

where the prefactor $\xi\left(d_{z'}\right) = \min\left\{1, \frac{dz'}{\sqrt{\pi}\left|W_{x'=0}\mathrm{erf}\left(\frac{L}{2W_{x'=0}}\right)\right|}\right\}$ takes into account the finiteness of the thickness of the microcrack array along the z' axis (note that $d_{z'} \equiv d$ in Fig. S2) and the finiteness of the incident beam width at $x' = 0$. The time dependence of (S10) is monochromatic, *i.e.*, $\mathrm{e}^{-\mathrm{i}2\pi f_0 t}$. To find the scattered field $p_{\text{sca}}(x', y')$, we first expand the plane wave and the scattered field into regular and singular cylindrical waves with the Bessel and first-kind Hankel functions, respectively,

$$\mathrm{e}^{-\mathrm{i}kx'} = \sum_{i,j,m} \mathcal{B}_{i,j,m} \underbrace{J_m(k|\mathbf{R}'_{ij}|)\mathrm{e}^{\mathrm{i}m\phi_{\mathbf{R}'_{ij}}}}_{\text{regular CWs}}, \quad p_{\text{sca}}(x', y') = \sum_{i,j,m} \mathcal{A}_{i,j,m} \underbrace{H_m^{(1)}(k|\mathbf{R}'_{ij}|)\mathrm{e}^{\mathrm{i}m\phi_{\mathbf{R}'_{ij}}}}_{\text{singular CWs}}, \tag{S11}$$

where $\sum_{i,j,m} \equiv \sum_{i=1}^{N_{x'}}\sum_{j=1}^{N_{y'}}\sum_{m=-1}^{1}$, $\mathbf{R}'_{ij} = (x' - x'_i, y' - y'_j, 0)$, $\phi_{\mathbf{R}'_{ij}} = \arctan\left[\frac{y'-y'_j}{x'-x'_i}\right]$, and the coefficients $\mathcal{B}_{i,j,m} = \mathrm{e}^{-\mathrm{i}kx'_i}(-\mathrm{i})^m$ (*43*). Next, we order coefficients $\mathcal{A}_{i,j,m}$ and $\mathcal{B}_{i,j,m}$ in vectors $\boldsymbol{\mathcal{A}}$ and $\boldsymbol{\mathcal{B}}$. Coefficients $\boldsymbol{\mathcal{B}}$ determine unknown coefficients $\boldsymbol{\mathcal{A}}$ via the following linear relationship $\boldsymbol{\mathcal{A}} = \boldsymbol{\mathcal{T}}\boldsymbol{\mathcal{B}}$ where $\boldsymbol{\mathcal{T}} = \left[\mathbf{I} - \boldsymbol{C}\boldsymbol{\mathcal{T}}_{\text{array}}\right]^{-1}\boldsymbol{\mathcal{T}}_{\text{array}}$. Here, we have constructed a block-diagonal matrix $\boldsymbol{\mathcal{T}}_{\text{array}}$ from matrix (S8) repeated $N_{x'} \times N_{y'}$ times, and matrix $\boldsymbol{C}$ contains singular translation coefficients that expand singular CWs into regular CWs at a different position $\mathbf{R}'' \neq \mathbf{R}'$ (*43*). Under normal incidence, the coefficients are given by $H_m^{(1)}(k|\mathbf{R}'|)\mathrm{e}^{\mathrm{i}m\phi_{\mathbf{R}'}} = \sum_{m'=-1}^{1} H_{m-m'}^{(1)}(k|\mathbf{R}' - \mathbf{R}''|)\mathrm{e}^{\mathrm{i}(m-m')\phi_{\mathbf{R}'-\mathbf{R}''}} J_{m'}(k|\mathbf{R}''|)\mathrm{e}^{\mathrm{i}m'\phi_{\mathbf{R}''}}$.

From (S10), we calculate the effective speed of sound as $v_i^{\text{eff}} = \left(\frac{\Delta\phi_i}{2\pi f_0 d_{x'}} + v_0^{-1}\right)^{-1}$, where $\Delta\phi_i$ is the phase shift of the total field $p\left(x'_{\text{M}}, y'_{\text{M}}\right)$ with respect to the incident field $p_{\text{inc}}\left(x'_{\text{M}}, y'_{\text{M}}\right)$ at a

given measurement point $\left(x'_{\mathrm{M}}, y'_{\mathrm{M}}\right)$, and then the effective density as $\rho_i^{\mathrm{eff}} = v_0\rho_0/v_i^{\mathrm{eff}}$. In Fig. S2, the measurement point is $(-\lambda, 0)$ when $x' = x$ and $x' = y$, and $(-3\lambda, 0)$ when $x' = z$. Note that the incident wave propagates along the $(-x')$ axis, and besides $x' = i$ where $i = x, y, z$ denotes one of the microcrack pattern axes.

Optimization of the laser engraving step

Several parameters were optimized to prevent the glass from shattering and the failure of the engraving process. First, the spacing between points was set to the minimum spacing suggested by the company, which is $[90, 90, 270]$ μm along the x, y, and z axes, respectively. For smaller spacings, the microcracks would merge and lead to major cracks. The spacing is bigger along the z axis because the microcracks are longer along this direction. Then, a safety margin of 4 mm was used between the side faces of the glass samples and the points. Eventually, the laser diode intensity was kept to 27.5 A. At higher values, the engraving process was more likely to fail because of large cracks emerging through the sample. At lower values, the engraved microcracks were too small (Fig. S1) and the acoustic properties of the effective medium were almost the same as those of the bulk medium (Fig. S11).

Potentially any 3D shape could be engraved as long as the engraving parameters are close to the ones described above.

Table S1: **Thermal properties of VeroClear and BK7 glass.** Comparison of thermal properties for VeroClear (*19, 44, 45*) and BK7 glass (*46*).

	VeroClear	BK7 glass
Glass transition temperature (°C)	54	557
Density ($\mathrm{kg\,m^{-3}}$)	1180	2510
Specific heat capacity ($\mathrm{J\,kg^{-1}\,K^{-1}}$)	1349	858
Volumetric heat capacity ($\mathrm{MJ\,K^{-1}\,m^{-3}}$)	1.59	2.15
Thermal conductivity ($\mathrm{W\,m^{-1}\,K^{-1}}$)	0.2261	1.1
Thermal expansion coefficient ($\mu\mathrm{m^{-1}\,m^{-1}\,°C^{-1}}$)	200	5.6

Table S2: **Parameters for the refracto-vibrometry measurements.** The setup involves a Polytec PSV 500 laser vibrometer, a signal generator, an amplifier, and an ultrasound transducer.

Vibrometer	Scanning head	PSV-I-500
	Laser wavelength	632.8 nm
	Acquisition mode	Time
	Sample length	500
	Sample frequency (MHz)	15.625
	Sample time (us)	32
	Resolution (ns)	64
	Optics	Close-up unit + micro scan lens (PSV-A-CL-200-HeNe)
	Field of view of the scanning area (mm)	40 x 40
	Spacing between scanning points	0.5 mm = $\lambda/5$
Signal generator	Signal	5-cycle burst centered at 2.25 MHz
	Voltage (V)	0.2
	Pulse Repetition Frequency (kHz)	1
Amplifier	Frequency range	10 kHz to 12 MHz
	Power gain (dB)	50
	Input and output impedance (ohms)	50
Transducer	Center frequency (MHz)	2.25
	Diameter (mm)	38.1 mm

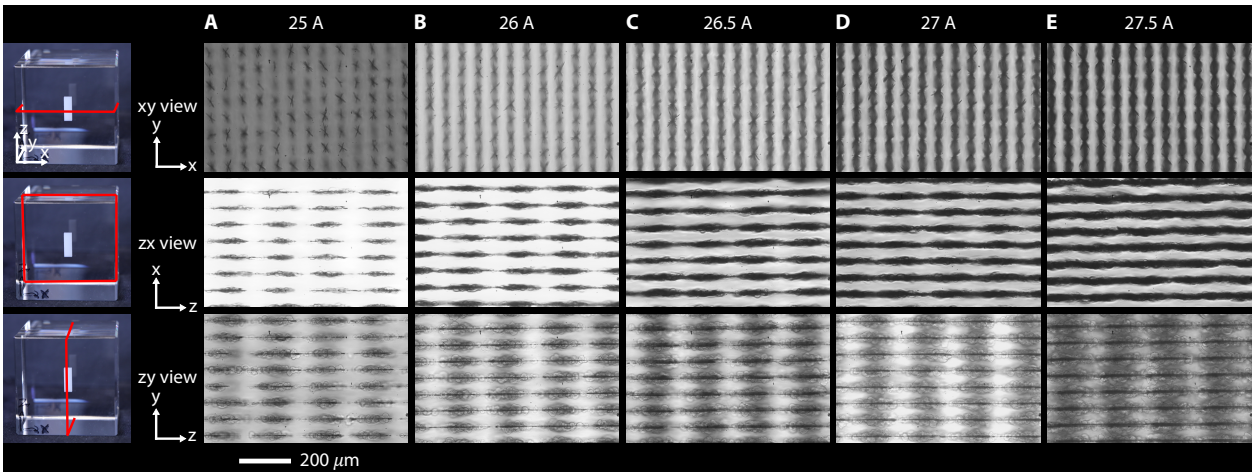


Figure S1: **Microscopy images of engraved microcracks for different laser currents.** Five samples were engraved with different laser diode currents of the pulsed laser: (**A**) 25 A, (**B**) 26 A, (**C**) 26.5 A, (**D**) 27 A, (**E**) 27.5 A. Three orthogonal views outlined in red (xy-top panel, zx-middle panel, and zy-bottom panel) were imaged with a bright-field microscope. The z axis is the direction of the engraving laser. The size of the microcracks increases with the laser diode intensity.

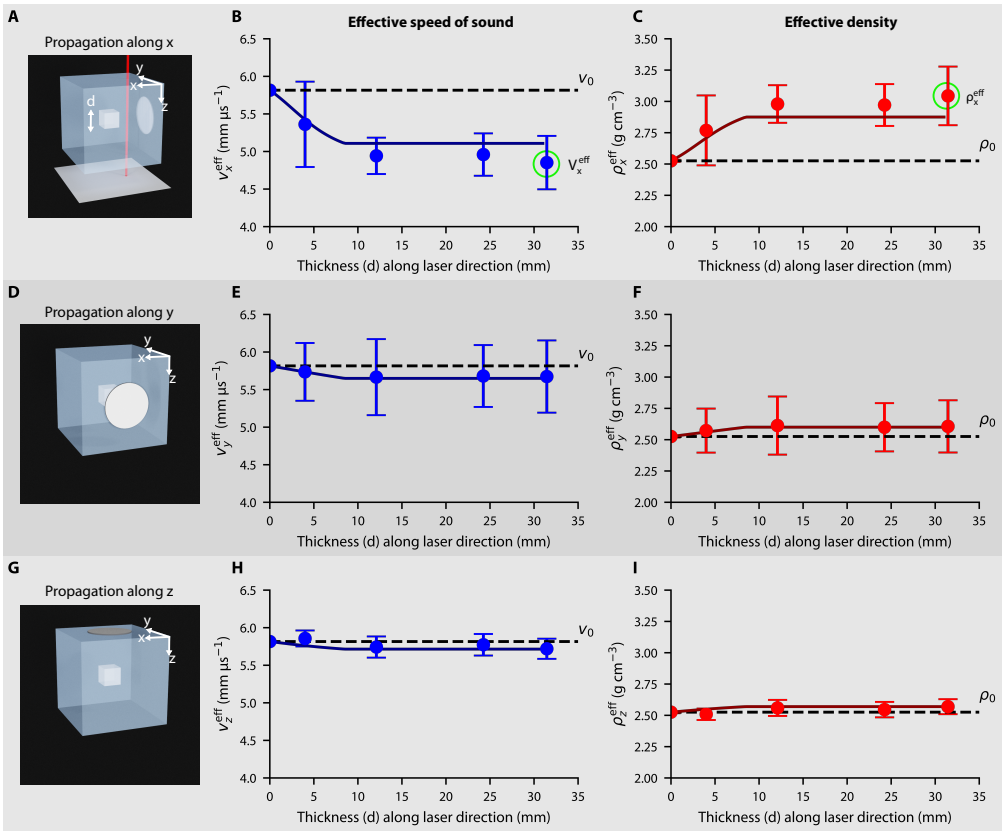


Figure S2: **Effective longitudinal speed of sound: T-matrix simulation and measurement.** With refracto-vibrometry measurements, a 3D sound field is reduced to a 2D projection. Therefore, the size of the engraved voxel along the vibrometry laser relative to the block size affects the measurement. The effective speed of sound and density were measured for different propagation directions (along x, y, or z). (**A**) Schematics of the setup for propagation along the x axis. (**B**) Effective speed of sound v_x^{eff} for different sizes of the engraved voxel d depicted in **A**. The T-matrix simulation data is depicted by a line, experimental refracto-vibrometry measurements by dots. The plot reaches a plateau value which is taken as the final value of v_x^{eff} (circle in green). For comparison, the speed of sound in the bulk medium v_0 is plotted with a horizontal dotted black line. (**C**) Effective density ρ_x^{eff} for different sizes of the engraved voxel. The plot reaches a plateau value which is taken as the final value of ρ_x^{eff} (circle in green). For comparison, the density in the bulk medium ρ_0 is plotted with a horizontal dotted black line. (**D**)-(**F**), same as (**A**)-(**C**) but for the ultrasound propagation along the y axis. (**G**)-(**I**), same as (**A**)-(**C**) but for the ultrasound propagation along the z axis

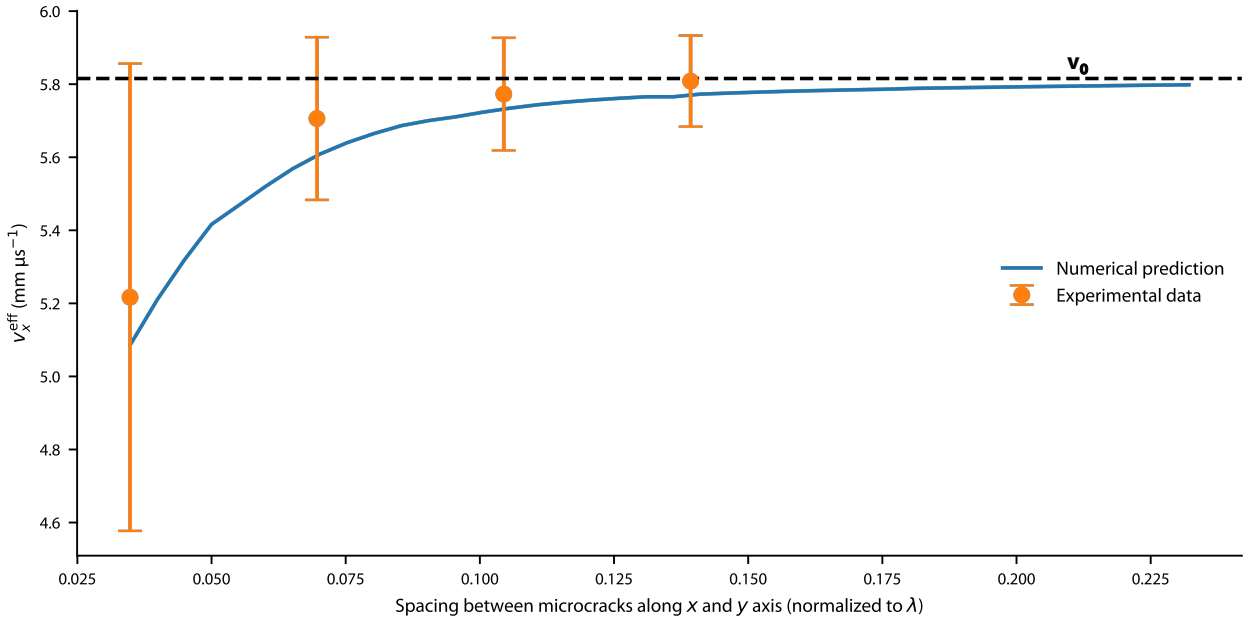


Figure S3: **Effective longitudinal speed of sound: measurement for different spacings.** The effective longitudinal speed of sound along the x axis was measured for engraved samples with different spacings between microcracks along the x and y axis. Experimental data points (mean $\pm$ std), shown by orange markers, confirm the prediction of the T-matrix method (blue solid line). The longitudinal speed of sound in the bulk medium v_0 is depicted by the horizontal black dashed line.

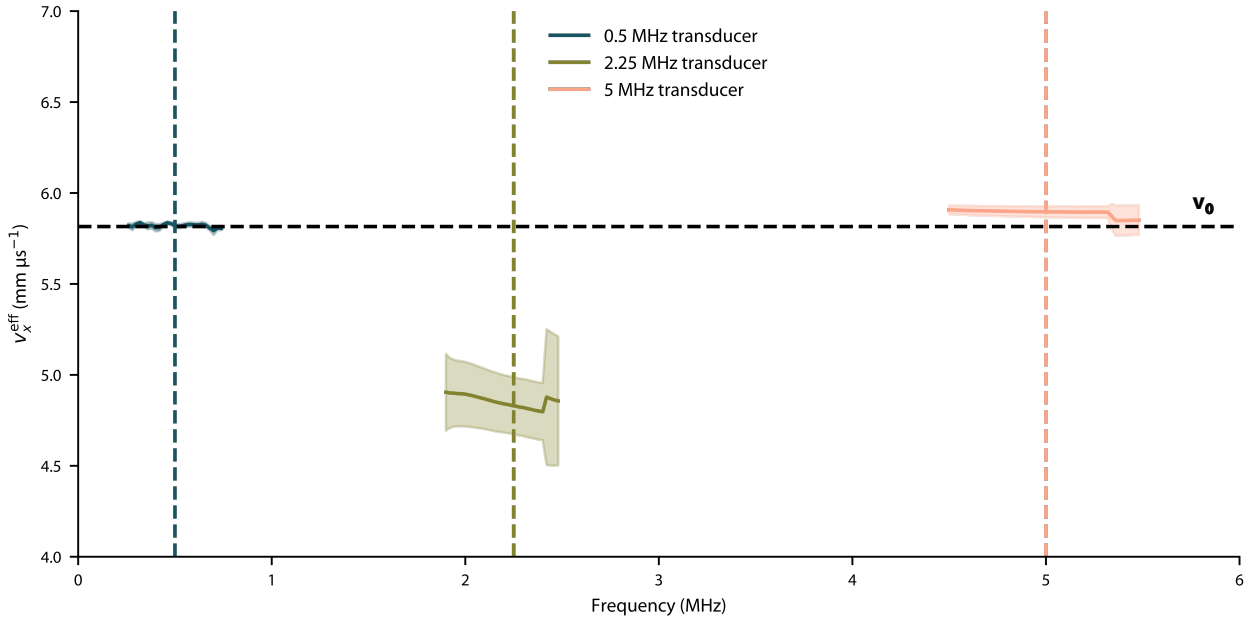


Figure S4: **Effective longitudinal speed of sound: measurement for different frequencies.** The effective longitudinal speed of sound along the x axis was measured using 3 transducers, whose center frequencies are 0.5, 2.25, and 5 MHz, respectively. Three vertical lines show these three center frequencies. The mean values are depicted by solid lines, ± *std* by the shadowed regions. The longitudinal speed of sound in the bulk medium v_0 is depicted by the horizontal black dashed line.

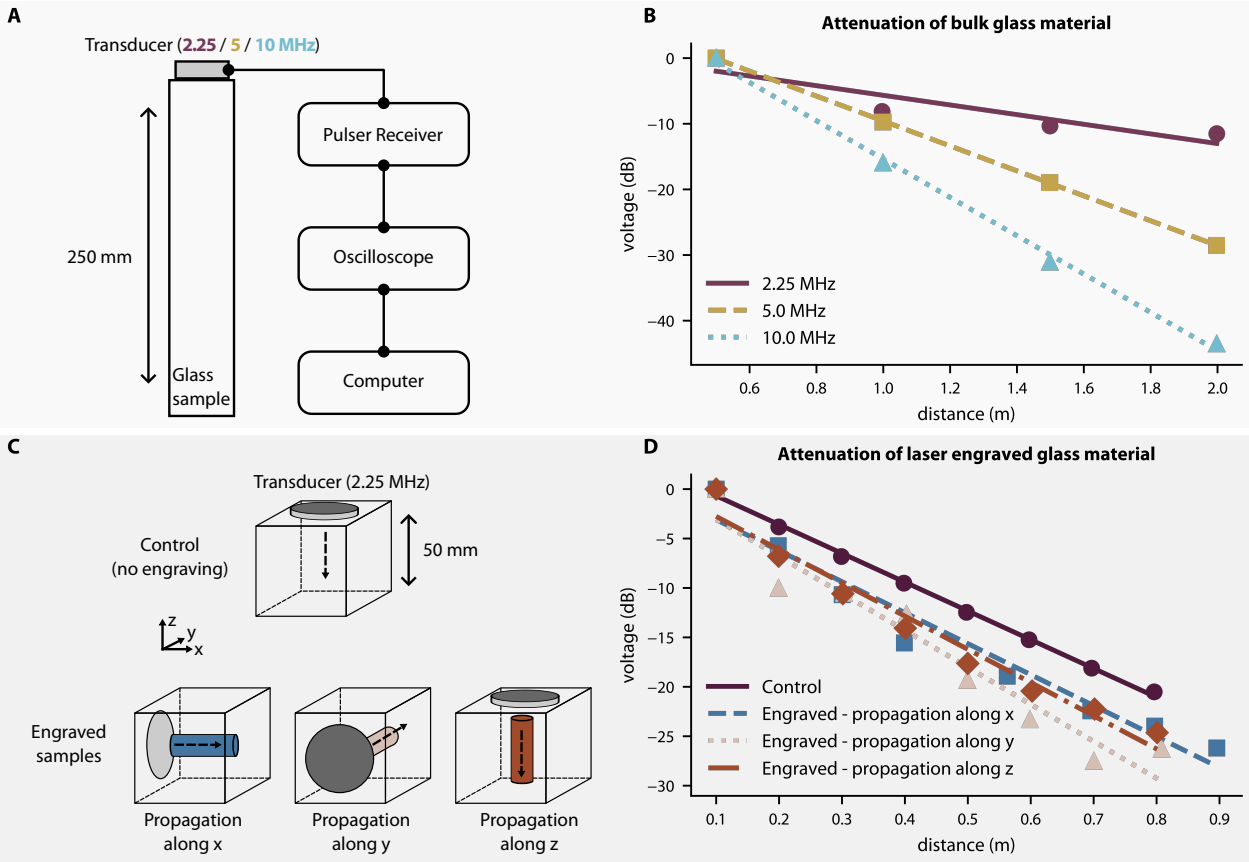


Figure S5: **Attenuation measurement of the bulk and engraved glass medium.** The attenuation inside the bulk medium (top panel) and inside the engraved medium (bottom panel) was measured. (**A**) Schematics of the experimental setup with a bigger glass block of size $70 \times 70 \times 250$ mm and a pulse-echo measurement. (**B**) The maximum absolute value of the signal in dB is plotted for different reflections, *i.e.*, different propagation distances. The amplitude decreases linearly with the distance at 2.25, 5, and 10 MHz. (**C**) Three glass cubes of size 50 mm were then engraved with a cylinder along the x, y, and z directions (with the z axis being the direction of the engraving laser). The attenuation was measured for each block and for a control block of the same size. (**D**) At 2.25 MHz, a 10%-higher attenuation is observed for the engraved blocks.

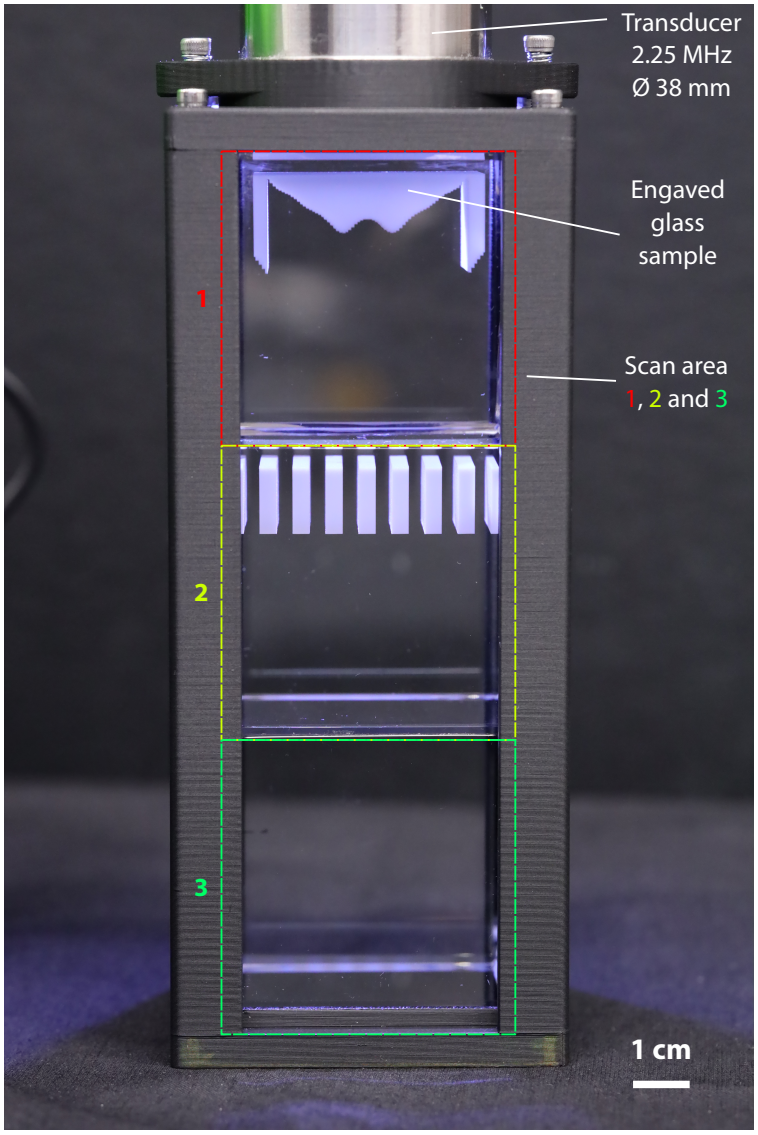


Figure S6: **Picture of the setup for the stacking of blocks.** 3D printed scaffold to align the stacked glass blocks. Two screws apply a light pressure between the blocks to reduce the acoustic reflection between the interfaces efficiently. Each scan area is outlined by a colored box. Scale bar is 1 cm.

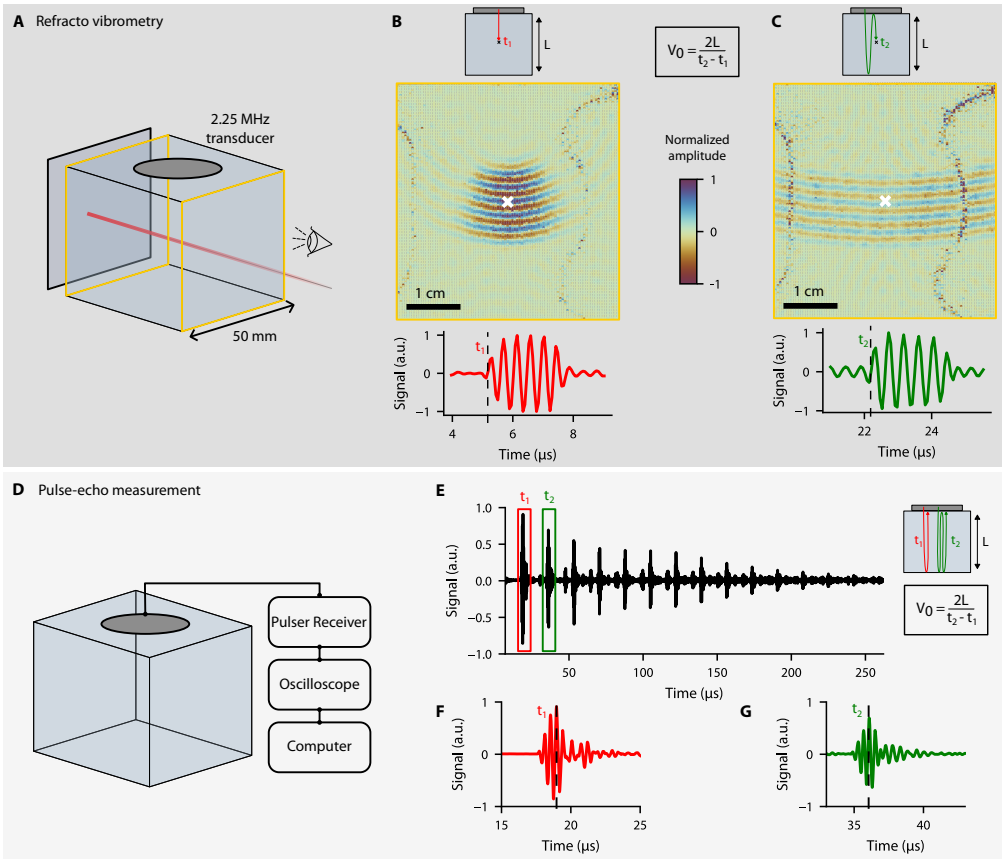


Figure S7: **Measurement of the speed of sound in the bulk medium.** It was measured with two techniques: refracto-vibrometry (top panel) and pulse-echo measurement (bottom panel). (**A**) Schematics of a refracto-vibrometry setup. A 3D sound field is reduced to a 2D projection. The eye and the highlighted faces of the cube depict the measurement direction. (**B**) Measurement of a control block (no engraving). A time profile from 1 scanning point (white cross) is plotted in red. Time of flight t_1 is indicated. (**C**) Signal after a reflection from the bottom and top faces of the cube. A time profile from the same scanning point is plotted in green. Time of flight t_2 is indicated. The equation used for the speed of sound calculation is outlined in black. (**D**) Schematics of the pulse-echo setup. (**E**) Plot of the measured signal over multiple reflections. (**F**) Subset of the signal (red box) for the first reflection. (**G**) Subset of the signal (green box) for the second reflection. Times of flight t_1 and t_2 for both signals are indicated. The equation used for the speed of sound calculation is outlined in black. All scale bars indicate 1 cm.

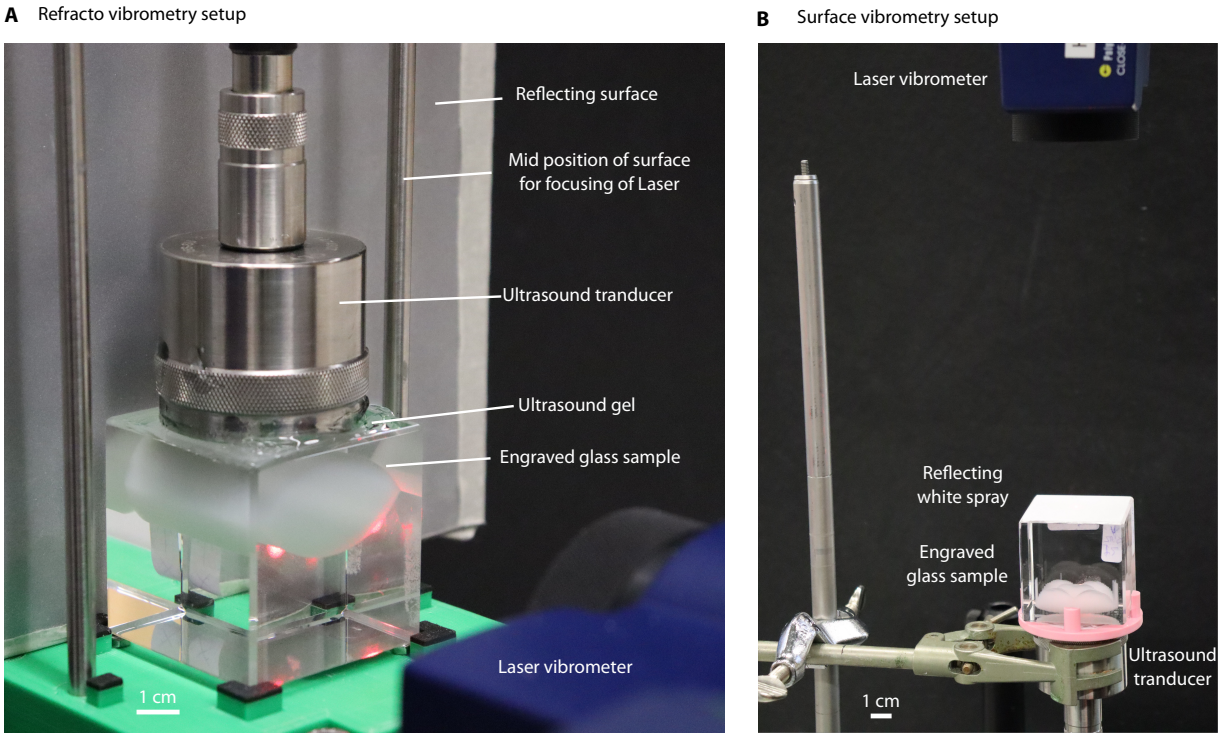


Figure S8: **Picture of the vibrometry setups.** Two vibrometry setups were used in this study. (**A**) A refracto-vibrometry technique scans a transparent block of glass while a 2.25 MHz burst is transmitted from the top face. (**B**) A standard surface vibrometry technique scans the vibration at the surface of one face opposite the transducer. All scale bars indicate 1 cm.

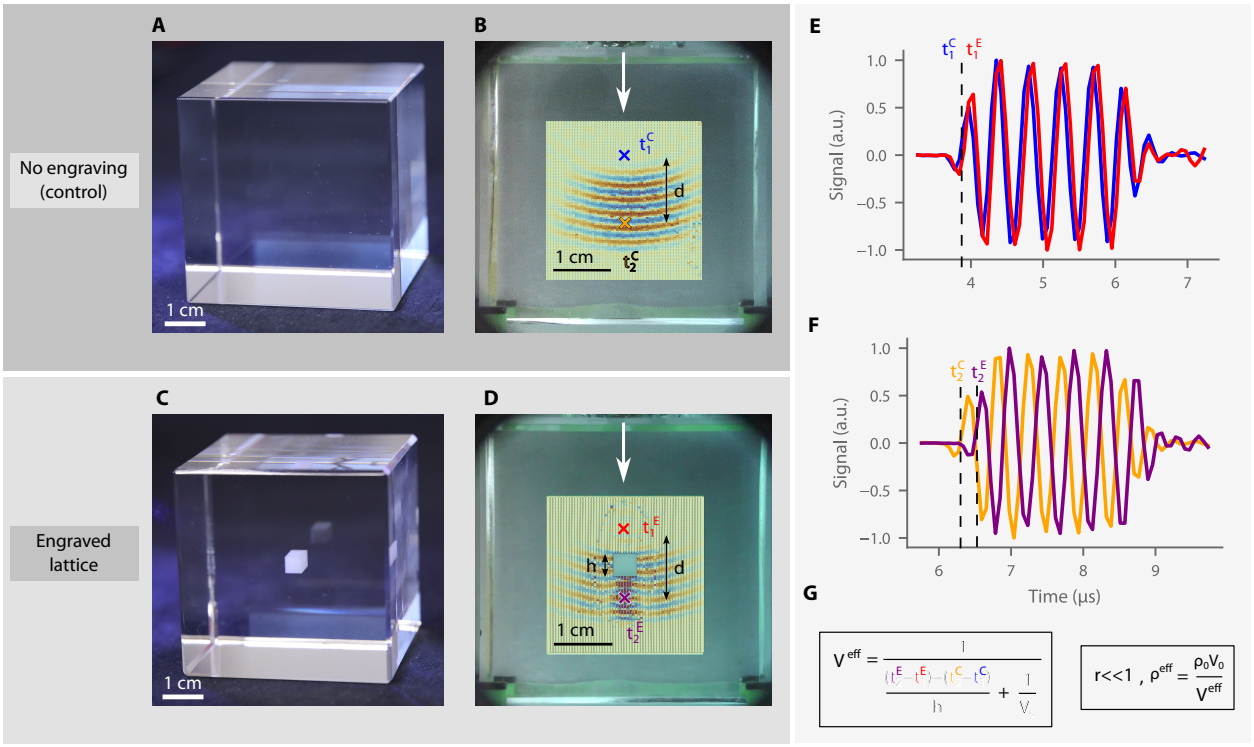


Figure S9: **Measurement of the effective longitudinal speed of sound.** For the measurement of the effective speed of sound, two samples were used: a control block (top panel) and a block with an engraved voxel at the center (bottom panel). (**A**) Picture of the control block. (**B**) The refracto-vibrometry signal. A white arrow depicts the propagation direction. (**C**) Picture of the engraved block. (**D**) Same as in (**B**) but for the engraved block. (**E**) Overlaid time signal for two scanning points (blue and red crosses). t_1^{C} and t_1^{E} are the time-of-flight for the control and engraved blocks, respectively. (**F**) Overlaid time signal for two scanning points (yellow and purple crosses). t_2^{C} and t_2^{E} are the time-of-flight for the control and engraved blocks, respectively. This time, a delay is observed when the sound propagates through the engraved voxel. The equations used for the effective speed of sound v^{eff} and the effective density ρ^{eff} calculation are outlined in black. They are functions of the times of flight, height of the engraved voxel h, and also ρ_0 and v_0, which are the density and speed of sound inside the bulk medium. For the density calculation, the pressure reflection coefficient was considered negligibly small $r \approx 0$. All scale bars indicate 1 cm.

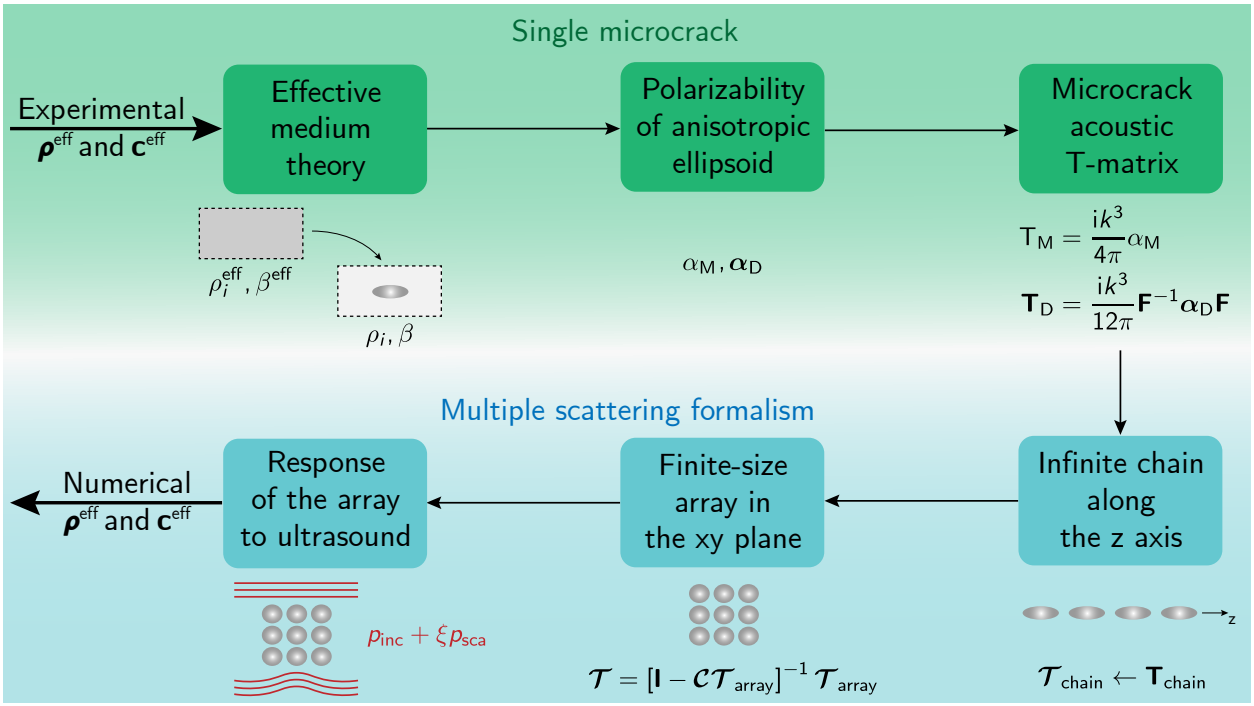


Figure S10: **Schematic illustration of the multi-step T-matrix-based numerical approach**. (A) We estimate the material parameters of a microcrack from the measured effective parameters utilizing an effective medium theory for noninteracting, diluted ellipsoids. (B) Using the material parameters, we compute the monopole and the dipole dynamic polarizabilities of a microcrack in the quasi-static approximation, considering it as an anisotropic ellipsoid, and (C) convert them to the T-matrix of a standalone microcrack. (D) From the microcrack T-matrix, we use the basis of scalar cylindrical waves to compute the T-matrix of a periodic chain, infinitely extended along the axis of refracto-vibrometry measurement (the z' axis). (E) In the $x'y'$ plane, we consider a given microcrack pattern as a finite 2D array of the chains and compute the T-matrix $\mathcal{T}$ that accounts for the mutual interaction between the chains. (F) At the final step, we use this T-matrix to map expansion coefficients of the incident field to expansion coefficients of the scattered field. The scattered field is then multiplied by the prefactor ξ that takes into account the finiteness of the pattern along the z' axis and the finiteness of the incident beam width at $x' = 0$.

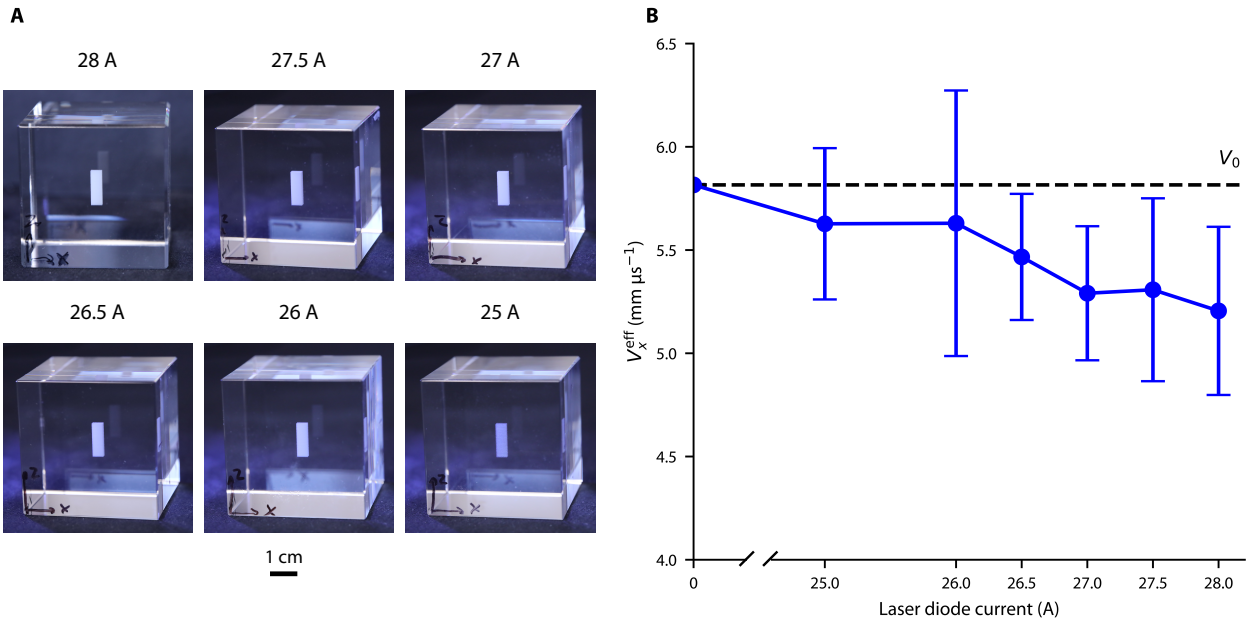


Figure S11: **Measurement of effective speed of sound for different laser diode currents.** Six samples were engraved with different laser diode currents of the pulsed laser. (**A**) Pictures of the different samples. (**B**) The effective speed of sound v_x^{eff} along the x axis was measured for the different laser diode currents. For comparison, the speed of sound in the bulk medium v_0 is plotted with a horizontal dotted black line. The effective speed of sound decreases with the laser intensity.